Partially averaged Navier-Stokes closure modeling for variable-density turbulent flow

F. S. Pereira,[1,*] F. F. Grinstein,[2] D. M. Israel,[2] R. Rauenzahn,[2] and S. S. Girimaji[3]
[1]*Los Alamos National Laboratory, T Division, Los Alamos, New Mexico 87545, USA*
[2]*Los Alamos National Laboratory, X Division, Los Alamos, New Mexico 87545, USA*
[3]*Texas A&M University, Ocean Engineering, College Station, Texas 77843, USA*

(Received 26 February 2021; accepted 16 July 2021; published 6 August 2021)

This work extends the framework of the partially averaged Navier-Stokes (PANS) equations to variable-density flow, i.e., multimaterial and/or compressible mixing problems with density variations and production of turbulence kinetic energy by both shear and buoyancy mechanisms. The proposed methodology is utilized to derive the PANS BHR-LEVM closure. This includes *a priori* testing to analyze and develop guidelines toward the efficient selection of the parameters controlling the physical resolution and, consequently, the range of resolved scales of PANS. Two archetypal test-cases involving transient turbulence, hydrodynamic instabilities, and coherent structures are used to illustrate the accuracy and potential of the method: the Taylor-Green vortex at Reynolds number $\mathrm{Re} = 3000$, and the Rayleigh-Taylor flow at Atwood number 0.5 and $(\mathrm{Re})_{\max} \approx 500$. These representative problems, for which turbulence is generated by shear and buoyancy processes, constitute the initial validation space of the new model, and their results are comprehensively discussed in two subsequent studies. The computations indicate that PANS can accurately predict the selected flow problems, resolving only a fraction of the scales of large-eddy simulation and direct numerical simulation strategies. The results also reiterate that the physical resolution of the PANS model must guarantee that the key instabilities and coherent structures of the flow are resolved. The remaining scales can be modeled through an adequate turbulence scale-dependent closure.

DOI: 10.1103/PhysRevFluids.6.084602

I. INTRODUCTION

The numerical prediction of variable-density (multimaterial and/or compressible) flows is crucial to numerous applications of fundamental and applied fluid mechanics, e.g., scramjets, mixing problems, oceanography, supernova explosions, and inertial confinement fusion. In addition to the shear production mechanism of constant density turbulence, variable-density flows include baroclinic production due to local mean density and pressure gradients. These flows are inherently transient and also include complex physics involving dilatation effects, characteristic hydrodynamic instabilities and coherent structures [1–6], and interactions between material and velocity fields. All these aspects make modeling and simulation of variable-density flows rife with challenges.

Direct numerical simulation (DNS) is the ideal option for prediction of any continuum fluid flow problem because it resolves all scales of motion. Large-eddy simulation (LES) [7], since it still resolves most of the turbulence spectrum, is expected to lead to accurate representations of the flow dynamics. Yet, such high-fidelity scale-resolving simulations (SRS) come with a computational

*fspereira@lanl.gov

expense that may be too prohibitive for practical applications. Also, selecting proper initial and boundary conditions for DNS and LES of variable-density problems is difficult.

The Reynolds-averaged Navier-Stokes (RANS) equations [8–12] are an alternative formulation to simulate practical flows of variable-density. In contrast to DNS and LES, RANS relies on a fully statistical description of turbulence, in which all turbulence scales are modeled through a constitutive relationship named turbulence closure [13–16]. This modeling strategy entails computation of the mean and coherent fields [17,18], and, consequently, significantly reduces the computations' cost. However, RANS closures are usually inaccurate, predicting many problems of interest in this study.

The caveats of the former modeling strategies drove the emergence of a new paradigm of practical SRS methods specially designed to predict complex flows efficiently. This class of models, named bridging methods, was proposed by Germano [19,20] and Speziale [21] to seamlessly operate between DNS and RANS, and only resolve the flow scales not amenable to modeling. The remaining scales can be accurately represented through an adequate closure [22]. This strategy is responsible for the potential efficiency (accuracy versus cost) of bridging methods, and it introduces the idea of accuracy-on-demand. Very large-eddy simulation (VLES) [21], limited numerical scales (LNS) [23], flow simulation methodology (FSM) [24], the partially integrated transport model (PITM) [25,26], and partially averaged Navier-Stokes (PANS) equations [27] are examples of bridging formulations.

Despite being widely used in many scientific areas, bridging models are still not common in the variable-density flow community. There are three main factors contributing to this outcome:

(i) *Complexity*. bridging closures are typically based on one-point RANS models, which are calibrated for total turbulent quantities. However, since bridging methods can operate at any range of resolved scales, the inability to reliably estimate RANS variables may lead to calibration deficiencies of the closure [28]. This is expected to be particularly relevant for low physical resolutions, transient and transitional flows, and second-moment closures [13–15,29,30]. Further, the RANS closures for variable-density flow possess terms to account for density variations that can be difficult to extend to the bridging framework.

(ii) *Physical resolution*. Bridging models normally require a physical resolution parameter, which determines the range of resolved scales and, consequently, the computational efficiency. This parameter defines the fraction of the dependent quantities of the turbulence closure being modeled, e.g., Reynolds-stress tensor, turbulence kinetic energy, dissipation, etc. Whereas excessively large physical resolutions increase the simulations range of resolved scales and cost unnecessarily, low values of such a parameter can lead to inaccurate computations. This makes the selection of the physical resolution crucial to the accuracy of the simulations.

A closure for variable-density flow will rely on multiple model evolution equations [14,15]. This raises the question of how different modeled turbulence quantities behave with the physical resolution. That is, what is the fraction of each dependent turbulence quantity being modeled for a given range of resolved scales? VLES, LNS, and FSM formulations use a pragmatic approach in which the magnitude of the Reynolds-stress tensor is scaled by a given factor. Despite being simple, this strategy does not yield the correct fixed point behavior for the closure system [31]. PANS and PITM, on the other hand, do not experience these issues since they use parameters to define the modeled-to-total ratio of each turbulence-dependent quantity. Yet, these ratios need to be defined in a physically consistent manner.

(iii) *Commutation errors*. SRS formulations are based upon the scale-invariance property of the Navier-Stokes equations [19]. This property is responsible for the formal similarity between the filtered Navier-Stokes and RANS equations, and it requires the implicit model filter operator to commute with temporal and spatial differentiation [19]. If this condition does not hold, the filtered Navier-Stokes equations have additional terms which are difficult to model and are often neglected. This creates the so-called commutation error [32,33].

Most SRS computations are conducted with a spatially varying physical resolution to optimize the use of the grid. Even for conventional LES models, this raises potential modeling issues (as

shown in [32]). For bridging models, such as PANS, spatial variation of the resolution control parameters leads to additional commutation terms [33], which can reach the magnitude of the convective terms of the filtered Navier-Stokes equations. This is expected to be relevant for variable-density turbulent flows due to their transient and transitional nature.

This work proposes a PANS bridging model specifically designed for variable-density turbulent flow. Thus, the PANS framework of Girimaji [27] and Suman and Girimaji [34] is extended to variable-density flow, and such a methodology is utilized to derive the PANS version of the six-equation BHR-LEVM (linear eddy viscosity model) closure [29,35]. In addition, we perform *a priori* testing to analyze and develop guidelines toward the efficient selection of the parameters controlling the physical resolution of the PANS model. The accuracy and potential of the model is evaluated through the prediction of two benchmark problems: the Taylor-Green vortex (TGV) [36] at Reynolds number (Re) 3000 and initial Mach number (Ma) 0.28, and the Rayleigh-Taylor flow [4,37] at Atwood number (At) 0.50, $(\mathrm{Re})_{\max} \approx 500$, and $\mathrm{Ma} < 0.10$. The first validation test-case assesses the ability of PANS BHR-LEVM to predict the onset and development of turbulence in a transient problem where turbulence is produced by shear processes. The second flow also includes multi-material mixing and turbulence produced by buoyancy mechanisms. These two canonical problems constitute the initial validation space [38,39] of the PANS BHR-LEVM model, and they are comprehensively analyzed in two subsequent studies [40,41]. All simulations are conducted at multiple physical resolutions to evaluate the effect of this parameter on the accuracy of the simulations. Also, the physical resolution is set constant in space and time to prevent commutation errors.

The remainder of this paper is structured as follows. Section II presents the derivation of the governing equations of PANS BHR-LEVM. A consistent framework and nomenclature is defined. Next, Sec. III analyzes the evolution of PANS turbulence-dependent quantities with the physical resolution, and it proposes guidelines toward the efficient selection of the parameters controlling the physical resolution of the model. Section IV describes the selected test-cases, while Sec. V discusses the main results. Section VI concludes this paper with a summary of the major findings.

II. GOVERNING EQUATIONS

The partially averaged Navier-Stokes (PANS) equations are based upon the scale-invariance property of the Navier-Stokes equations. This property has been demonstrated by Germano [19] for incompressible flow, and extended to compressible flow by Suman and Girimaji [34]. To derive the PANS equations for variable-density flow (multimaterial and/or compressible), let us start by considering a general linear and constant preserving filtering operator $\langle \cdot \rangle$,

$$\langle \Phi_1 + \Phi_2 \rangle = \langle \Phi_1 \rangle + \langle \Phi_2 \rangle, \tag{1}$$

$$\langle \alpha \Phi \rangle = \alpha \langle \Phi \rangle, \tag{2}$$

where Φ is a generic variable, and α is a constant. This filter commutes with spatial and temporal differentiation so that

$$\left\langle \frac{\partial \Phi}{\partial x_i} \right\rangle = \frac{\partial \langle \Phi \rangle}{\partial x_i}, \quad \left\langle \frac{\partial \Phi}{\partial t} \right\rangle = \frac{\partial \langle \Phi \rangle}{\partial t}, \tag{3}$$

and it decomposes any instantaneous flow quantity Φ into a filtered (resolved), $\langle \Phi \rangle$, and modeled (unresolved), ϕ, component,

$$\Phi \equiv \langle \Phi \rangle + \phi. \tag{4}$$

This decomposition can be extended to variable-density flow through the concept of Favre-averaging [9–12],

$$\Phi \equiv \{\Phi\} + \phi^*, \tag{5}$$

where $\{\Phi\}$ and ϕ^* are the density-weighted filtered, $\{\Phi\} \equiv \langle\rho\Phi\rangle/\langle\rho\rangle$, and modeled fluctuating, $\phi^* = \Phi - \{\Phi\}$, components of Φ. In the limit of all turbulence scales being modeled, the former decompositions are equivalent to Reynolds- [8] and Favre-averaging [9–12],

$$\Phi = \overline{\Phi} + \phi', \tag{6}$$

$$\Phi = \tilde{\Phi} + \phi'', \tag{7}$$

$\overline{\Phi}$ and ϕ' being the (time, ensemble, or spatial) averaged and turbulent components of Φ, whereas $\tilde{\Phi}$ and ϕ'' are the density-weighted averaged and fluctuating counterparts of Φ.

The application of such filtering operators to the conservation equations for mass, momentum, total energy, and fluid species [42,43] leads to the filtered or partially averaged form of the Navier-Stokes equations for variable-density flow [19,27,34,40],

$$\frac{\partial\langle\rho\rangle}{\partial t} + \frac{\partial(\langle\rho\rangle\{V_i\})}{\partial x_i} = 0, \tag{8}$$

$$\begin{aligned}\frac{\partial(\langle\rho\rangle\{V_i\})}{\partial t} + \frac{\partial(\langle\rho\rangle\{V_j\}\{V_i\})}{\partial x_j} &= -\frac{\partial\langle P\rangle}{\partial x_i} + \frac{\partial\langle\sigma_{ij}\rangle}{\partial x_j} \\ &\quad + \frac{\partial[\langle\rho\rangle\tau^1(V_i, V_j)]}{\partial x_j} + \langle\rho\rangle g_i,\end{aligned} \tag{9}$$

$$\begin{aligned}\frac{\partial(\langle\rho\rangle\{E\})}{\partial t} + \frac{\partial(\langle\rho\rangle\{E\}\{V_j\})}{\partial x_j} &= -\frac{\partial[\langle\rho\rangle\tau^1(V_j, E)]}{\partial x_j} \\ &\quad - \frac{\partial(\{V_j\}\langle P\rangle)}{\partial x_j} - \frac{\partial\tau^2(V_j, P)}{\partial x_j} \\ &\quad + \frac{\partial(\{V_i\}\langle\sigma_{ij}\rangle)}{\partial x_j} + \frac{\partial\tau^2(V_i, \sigma_{ij})}{\partial x_j} \\ &\quad - \frac{\partial\langle q_j^c\rangle}{\partial x_j} - \frac{\partial\langle q_j^h\rangle}{\partial x_j}\end{aligned} \tag{10}$$

$$\frac{\partial(\langle\rho\rangle\{c^n\})}{\partial t} + \frac{\partial(\langle\rho\rangle\{c^n\}\{V_j\})}{\partial x_j} = -\frac{\partial\langle J_j^n\rangle}{\partial x_j}. \tag{11}$$

Here, t is the time, x_i are the coordinates of a Cartesian system, ρ is the fluid density, V_i are the Cartesian velocity components, P is the pressure, σ_{ij} is the viscous-stress tensor assuming Newtonian fluid,

$$\langle\sigma_{ij}\rangle = 2\mu\left(\{S_{ij}\} - \frac{2}{3}\frac{\partial\{V_k\}}{\partial x_k}\delta_{ij}\right), \tag{12}$$

$\{S_{ij}\}$ is the resolved strain-rate tensor,

$$\{S_{ij}\} = \frac{1}{2}\left(\frac{\partial\{V_i\}}{\partial x_j} + \frac{\partial\{V_j\}}{\partial x_i}\right), \tag{13}$$

μ is the fluid's dynamic viscosity, δ_{ij} is the Kronecker delta, g_i is the gravitational acceleration vector, $E = \frac{1}{2}V_i^2 + e$ is the total energy of the fluid, e is the internal energy, c^n is the mass concentration of material n, q^c is the conductive heat flux, q^d is the interdiffusional enthalpy flux, and J^n is the mass fraction diffusivity flux of material n. Also, $\tau^1(\Phi_i, \Phi_j)$ and $\tau^2(\Phi_i, \Phi_j)$ are generalized central second moments which account for the effect of the modeled turbulence in the

resolved flow field. Expressing the PANS equations in terms of generalized central second moments [19] guarantees scale-invariance. Such tensors are formally defined as [19,34]

$$\tau^1(\Phi_i, \Phi_j) \equiv \{\Phi_i \Phi_j\} - \{\Phi_i\}\{\Phi_j\}, \tag{14}$$

$$\tau^2(\Phi_i, \Phi_j) \equiv \langle \Phi_i \Phi_j \rangle - \{\Phi_i\}\langle \Phi_j \rangle. \tag{15}$$

In Eqs. (8)–(11), the pressure is calculated assuming a thermally perfect gas ($P = \rho RT$). Thus, its resolved component is given by [34]

$$\langle P \rangle = (\gamma - 1)\langle \rho \rangle \left(\{E\} - \frac{\{V_k\}\{V_k\}}{2} - k_u \right), \tag{16}$$

where T is the temperature, γ is the ratio between specific heats, and k_u is the unresolved or modeled specific turbulence kinetic energy.

The generalized central second moments and fluxes present in the PANS equations need modeling to close the resultant system of equations. In the present work, this is accomplished through the Boussinesq approximation [44],

$$\tau^1(V_i, V_j) = 2\nu_u \{S_{ij}\} - \tfrac{2}{3} k_u \delta_{ij}, \tag{17}$$

and the relationships given in [13,29,30,34]. These lead to the partially averaged form of the energy and fluid species equations,

$$\begin{aligned} &\frac{\partial(\langle \rho \rangle \{E\})}{\partial t} + \frac{\partial(\langle \rho \rangle \{E\}\{V_j\})}{\partial x_j} \\ &= -\frac{\partial(\{V_j\}\langle P \rangle)}{\partial x_j} + \frac{\partial(\{V_i\}\langle \sigma_{ij} \rangle)}{\partial x_j} + \frac{\partial[\langle \rho \rangle \{V_i\} \tau^1(V_i, V_j)]}{\partial x_j} + \frac{\partial}{\partial x_j}\left[\left(\mu + \frac{\mu_u}{\sigma_k} \right) \frac{\partial k_u}{\partial x_j} \right] \\ &\quad - \frac{\partial}{\partial x_j}\left[c_p \left(\frac{\mu}{\mathrm{Pr}} + \frac{\mu_u}{\mathrm{Pr}_t} \right) \frac{\partial \langle T \rangle}{\partial x_j} \right] - \frac{\partial}{\partial x_j}\left[\sum_{n=1}^{n_t} h_n \langle J_j^n \rangle \right], \end{aligned} \tag{18}$$

$$\frac{\partial(\langle \rho \rangle \{c^n\})}{\partial t} + \frac{\partial(\langle \rho \rangle \{c^n\}\{V_j\})}{\partial x_j} = -\frac{\partial \langle J_j^n \rangle}{\partial x_j} = -\frac{\partial}{\partial x_j}\left[\langle \rho \rangle \left(\mathcal{D} + \frac{\nu_u}{\sigma_c} \right) \frac{\partial \{c^n\}}{\partial x_j} \right], \tag{19}$$

where $\nu_u = \mu_u / \langle \rho \rangle$ is the kinematic turbulent viscosity of the unresolved scales, σ_k and σ_c are turbulent diffusion coefficients, c_v is the constant specific heat (ideal gas is assumed), Pr is the Prandtl number, $\mathrm{Pr_t}$ is the turbulent Prandtl number defined as $\mathrm{Pr_t} = c_v \nu_u / \kappa$, κ is the effective thermal conductivity, and h^n is the enthalpy of material n. Throughout this manuscript, all modeled/unresolved PANS and RANS turbulence quantities are denoted by the subscripts u and t, respectively.

The relationships above create two additional turbulence quantities, k_u and ν_u, that need modeling. This is accomplished through the BHR-LEVM [29,35] closure model, which is now derived for PANS.

A. PANS BHR-LEVM closure

Most PANS closures are based on one-point, linear turbulent viscosity RANS closures. This modeling strategy is chosen to balance sufficient complexity to accurately operate at any degree of physical resolution with scale-aware minor modifications [45], without the loss of robustness observed for full Reynolds-stress closures. For variable-density flow we choose the BHR model originally proposed by Besnard *et al.* [13], in k_t-S_t linear turbulent viscosity form found in [29,35]. The model requires transport equations for six turbulence-dependent variables: the turbulence

TABLE I. Coefficients of BHR-LEVM closure [29].

c_1	c_2	c_4	c_{a_1}	c_b	c_μ	σ_a	σ_b	σ_c	σ_k	σ_S
0.06	0.42	0.45	6.00	0.45	0.28	1.00	3.00	0.60	1.00	0.10

kinetic energy, k_t, turbulence dissipation length-scale, S_t, velocity mass flux, a_{i_t},

$$a_{i_t} = \frac{\overline{\rho' v_i'}}{\overline{\rho}}, \tag{20}$$

and density-specific volume correlation, b_t,

$$b_t = -\overline{\rho'(1/\rho)'}. \tag{21}$$

In Eqs. (20) and (21), the primes refer to the fluctuating component over the mean value so that these quantities can be divided into a coherent and turbulent part [46]. For the b_t equation, we use the newer formulation of Schwarzkopf *et al.* [47]. The subscript t indicates a total turbulence quantity, that is, the quantity predicted by the RANS model that includes the action of all the turbulent scales of motion. The subscript u will be used for partial-averaged quantities, including only the unresolved portion of the turbulent scales.

The RANS BHR-LEVM model used in this work calculates the total kinematic turbulent viscosity as

$$\nu_t = \frac{\mu_t}{\overline{\rho}} = c_\mu S_t \sqrt{k_t}, \tag{22}$$

where c_μ is a coefficient given in Table I, and S_t is the turbulence dissipation length-scale defined as

$$S_t = \frac{k_t^{3/2}}{\varepsilon_t}, \tag{23}$$

and ε_t is the specific total turbulence dissipation. The turbulence quantities k_t and S_t are obtained from the following evolution equations:

$$\frac{\partial \overline{\rho} k_t}{\partial t} + \frac{\partial \overline{\rho} k_t \tilde{V}_j}{\partial x_j} = \mathcal{P}_{b_t} + \mathcal{P}_{s_t} - \overline{\rho}\frac{k_t^{3/2}}{S_t} + \frac{\partial}{\partial x_j}\left(\frac{\overline{\rho}\nu_t}{\sigma_k}\frac{\partial k_t}{\partial x_j}\right), \tag{24}$$

$$\frac{\partial \overline{\rho} S_t}{\partial t} + \frac{\partial \overline{\rho} S_t \tilde{V}_j}{\partial x_j} = \frac{S_t}{k_t}\left(c_4 \mathcal{P}_{b_t} + c_1 \mathcal{P}_{s_t}\right) - \overline{\rho} c_2 \sqrt{k_t} + \frac{\partial}{\partial x_j}\left(\frac{\overline{\rho}\nu_t}{\sigma_S}\frac{\partial S_t}{\partial x_j}\right), \tag{25}$$

$$\frac{\partial \overline{\rho} a_{i_t}}{\partial t} + \frac{\partial \overline{\rho} a_{i_t} \tilde{V}_j}{\partial x_j} = b_t \frac{\partial \overline{P}}{\partial x_i} + R^1(V_i, V_j)\frac{\partial \overline{\rho}}{\partial x_j} + \overline{\rho}\frac{\partial (a_{i_t} a_{j_t})}{\partial x_j} - c_{a_1}\overline{\rho} a_{i_t}\frac{\sqrt{k_t}}{S_t}$$
$$- \overline{\rho} a_{j_t}\frac{\partial \overline{V}_i}{\partial x_j} + \frac{\partial}{\partial x_j}\left(\frac{\overline{\rho}\nu_t}{\sigma_a}\frac{\partial a_{i_t}}{\partial x_j}\right), \tag{26}$$

$$\frac{\partial \overline{\rho} b_t}{\partial t} + \frac{\partial \overline{\rho} b_t \tilde{V}_j}{\partial x_j} = 2\overline{\rho} a_{j_t}\frac{\partial b_t}{\partial x_j} - 2a_{j_t}(b_t + 1)\frac{\partial \overline{\rho}}{\partial x_j} - c_b \overline{\rho} b_t \frac{\sqrt{k_t}}{S_t} + \overline{\rho}^2 \frac{\partial}{\partial x_j}\left(\frac{\nu_t}{\overline{\rho}\sigma_b}\frac{\partial b_t}{\partial x_j}\right), \tag{27}$$

where $\mathcal{P}_{b_t}$ and $\mathcal{P}_{s_t}$ are the specific total production of turbulence kinetic energy by buoyancy and shear mechanisms,

$$\mathcal{P}_{b_t} = a_{j_t}\frac{\partial \overline{P}}{\partial x_j}, \tag{28}$$

$$\mathcal{P}_{s_t} = -\overline{\rho} R^1(V_i, V_j)\frac{\partial \tilde{V}_i}{\partial x_j}, \tag{29}$$

$R^1(V_i, V_j)$ is the Reynolds stress tensor [$R^1(V_i, V_j)$ and $\tau^1(V_i, V_j)$ are equivalent when all turbulence scales are modeled], and c_1, c_2, c_4, c_{a_1}, c_b, σ_k, σ_S, σ_a, and σ_b are coefficients of the original RANS BHR-LEVM model, whose values are given in Table I.

Equations (24)–(27) have been designed to operate exclusively with RANS variables: Reynolds averaged, $\overline{\Phi}$, density-weighted averaged, $\tilde{\Phi}$, and total turbulence, Φ_t, quantities. We now derive their PANS counterpart by extending the framework proposed by Girimaji [27] to variable-density flow. To this end, the parameters f_ϕ defining the ratios of modeled-to-total specific turbulence kinetic energy, f_k, dissipation length-scale, f_S, mass flux velocity, f_{a_i}, and density-specific volume correlation, f_b,

$$f_k \equiv \frac{k_u}{k_t}, \quad f_S \equiv \frac{S_u}{S_t}, \quad f_{a_i} \equiv \frac{a_{i_u}}{a_{i_t}}, \quad f_b \equiv \frac{b_u}{b_t}, \tag{30}$$

need to be included in Eqs. (24)–(27). These define the physical resolution and, as such, the fraction of the dependent quantities of the turbulent closure being modeled. Also, they enable the closure to operate at any range of resolved scales, i.e., from RANS ($f_\phi = 1$), where turbulence is fully represented by the closure so that $\tau^1(V_i, V_j) = R^1(V_i, V_j)$, to DNS ($f_\phi = 0$, no closure), where turbulence is fully resolved so that $\tau^1(V_i, V_j) = 0$. f_S can also be calculated as a function of f_k and f_ε,

$$f_S \equiv \frac{S_u}{S_t} = \left(\frac{k_u^{3/2}}{\varepsilon_u}\right)\left(\frac{\varepsilon_t}{k_t^{3/2}}\right) = \frac{f_k^{3/2}}{f_\varepsilon}, \tag{31}$$

where f_ε is the ratio of modeled-to-total specific turbulence dissipation. Since f_ε is physically more intuitive than f_S, the evolution equations for k_u, S_u, a_{i_u}, and b_u are derived in terms of f_k, f_ε, f_{a_i}, and f_b.

1. k_u evolution equation

It has been demonstrated by Girimaji [27] and Suman and Girimaji [34] that the scale-invariant form of the k_u equation can be written as

$$\frac{\partial \langle\rho\rangle k_u}{\partial t} + \frac{\partial \langle\rho\rangle k_u \{V_j\}}{\partial x_j} = \mathcal{P}_{b_u} + \mathcal{P}_{s_u} - \mathcal{E}_u + \mathcal{T}_u, \tag{32}$$

where $\mathcal{P}_{b_u}$ and $\mathcal{P}_{s_u}$ are the production of k_u by buoyancy and shear mechanisms,

$$\mathcal{P}_{b_u} = a_{j_u} \frac{\partial \langle P\rangle}{\partial x_j}, \tag{33}$$

$$\mathcal{P}_{s_u} = -\langle\rho\rangle \tau^1(V_i, V_j) \frac{\partial \{V_i\}}{\partial x_j}, \tag{34}$$

and $\mathcal{E}_u = \langle\rho\rangle \varepsilon_u$ and $\mathcal{T}_u$ represent the dissipation and transport of modeled turbulence kinetic energy. For constant f_k, differentiation commutes in time and space and so it possible to establish a relationship between the equations for k_u (PANS) and k_t (RANS),

$$\frac{\partial \overline{\rho} k_u}{\partial t} + \frac{\partial \overline{\rho} k_u \tilde{V}_j}{\partial x_j} = f_k \left[\frac{\partial \overline{\rho} k_t}{\partial t} + \frac{\partial \overline{\rho} k_t \tilde{V}_j}{\partial x_j}\right]. \tag{35}$$

Since PANS calculates filtered or partially averaged dependent variables, the former relationship can be rewritten as follows:

$$\frac{\partial \overline{\rho} k_u}{\partial t} + \frac{\partial \overline{\rho} k_u \{V_j\}}{\partial x_j} = f_k \left[\frac{\partial \overline{\rho} k_t}{\partial t} + \frac{\partial \overline{\rho} k_t \tilde{V}_j}{\partial x_j}\right] + \frac{\partial}{\partial x_j}[k_u \overline{\rho}(\{V_j\} - \tilde{V}_j)]. \tag{36}$$

Next, replacing the term between brackets by the right-hand side of Eq. (24) and introducing the parameter $f_\rho = \langle\rho\rangle/\overline{\rho}$ leads to

$$\frac{\partial\langle\rho\rangle k_u}{\partial t} + \frac{\partial\langle\rho\rangle k_u\{V_j\}}{\partial x_j} = f_\rho f_k\left[\mathcal{P}_{b_t} + \mathcal{P}_{s_t} - \mathcal{E}_t + \mathcal{T}_t\right] + \frac{\partial}{\partial x_j}[k_u\langle\rho\rangle(\{V_j\} - \tilde{V}_j)], \tag{37}$$

and applying self-similarity considerations to the left-hand side, the following relation is obtained:

$$\mathcal{P}_{b_u} + \mathcal{P}_{s_u} - \mathcal{E}_u + \mathcal{T}_u = f_\rho f_k\left[\mathcal{P}_{b_t} + \mathcal{P}_{s_t} - \mathcal{E}_t + \mathcal{T}_t\right] + \frac{\partial}{\partial x_j}[k_u\langle\rho\rangle(\{V_j\} - \tilde{V}_j)]. \tag{38}$$

This equation shows the formal similarity between PANS (left-hand side) and RANS (right-hand side) production, dissipation, and transport terms. Hence, it is possible to relate the source and sink (local processes) and transport terms as follows:

$$\mathcal{P}_{b_u} + \mathcal{P}_{s_u} - \mathcal{E}_u = f_\rho f_k\left[\mathcal{P}_{b_t} + \mathcal{P}_{s_t} - \mathcal{E}_t\right], \tag{39a}$$

$$\mathcal{T}_u = f_\rho f_k \mathcal{T}_t + \frac{\partial}{\partial x_j}[k_u\langle\rho\rangle(\{V_j\} - \tilde{V}_j)]. \tag{39b}$$

Now, we define the weighting functions ω_s and ω_b,

$$\omega_s = \frac{\mathcal{P}_{s_u}}{\mathcal{P}_{b_u} + \mathcal{P}_{s_u}}, \tag{40}$$

$$\omega_b = \frac{\mathcal{P}_{b_u}}{\mathcal{P}_{b_u} + \mathcal{P}_{s_u}}, \tag{41}$$

which define the relative weight of the shear, ω_s, and buoyancy, ω_b, mechanisms to the total production of specific turbulence kinetic energy. Thus, their sum is equal to unity, $\omega_s + \omega_b = 1$. Using f_k, f_ε and these weighting functions, we can rewrite Eq. (39a),

$$\mathcal{P}_{b_u} + \mathcal{P}_{s_u} - \mathcal{E}_u\omega_s - \mathcal{E}_u\omega_b = f_k\left[f_\rho\left(\mathcal{P}_{b_t} + \mathcal{P}_{s_t}\right) - \omega_s\frac{\mathcal{E}_u}{f_\varepsilon} - \omega_b\frac{\mathcal{E}_u}{f_\varepsilon}\right], \tag{42}$$

and obtain the relationships

$$f_\rho\mathcal{P}_{b_t} = \frac{\mathcal{P}_{b_u}}{f_k} - \omega_b\mathcal{E}_u\left(\frac{1}{f_k} - \frac{1}{f_\varepsilon}\right), \tag{43}$$

$$f_\rho\mathcal{P}_{s_t} = \frac{\mathcal{P}_{s_u}}{f_k} - \omega_s\mathcal{E}_u\left(\frac{1}{f_k} - \frac{1}{f_\varepsilon}\right). \tag{44}$$

The former relations are used to derive the evolution equation for S_u. On the other hand, the transport terms of the k_u and k_t equations can be related as follows:

$$\begin{aligned}\mathcal{T}_u &= f_\rho f_k[\mathcal{T}_t] + \frac{\partial}{\partial x_j}[k_u\langle\rho\rangle(\{V_j\} - \tilde{V}_j)] \\ &= f_\rho f_k\left[\frac{\partial}{\partial x_j}\left(\frac{\overline{\rho}\nu_t}{\sigma_k}\frac{\partial k_t}{\partial x_j}\right)\right] + \frac{\partial}{\partial x_j}[k_u\langle\rho\rangle(\{V_j\} - \tilde{V}_j)] \\ &= \frac{\partial}{\partial x_j}\left(\frac{\langle\rho\rangle\nu_u}{\sigma_k}\frac{f_\varepsilon}{f_k^2}\frac{\partial k_u}{\partial x_j}\right) + \frac{\partial}{\partial x_j}[k_u\langle\rho\rangle(\{V_j\} - \tilde{V}_j)],\end{aligned} \tag{45}$$

where $\nu_u = c_\mu S_u\sqrt{k_u}$. Using scaling arguments, Girimaji [27] showed that

$$\frac{\partial}{\partial x_j}[k_u\langle\rho\rangle(\{V_j\} - \tilde{V}_j)] \approx 0, \tag{46}$$

leading to the so-called zero-transport model (ZTM). The accuracy of this model has been confirmed in the recent study of Tazraei and Girimaji [48]. Also, it is important to highlight that the velocity

difference term tends to zero in the limit of $f_k = 0.00$ and 1.00 since

$$k_u = 0 \text{ at } f_k = 0.0, \qquad \{V_j\} - \tilde{V}_j = 0 \text{ at } f_k = 1.0. \tag{47}$$

The derivation of the evolution equation for k_u concludes by combining Eqs. (37), (45), and (46). This leads to its final form,

$$\frac{\partial \langle\rho\rangle k_u}{\partial t} + \frac{\partial \langle\rho\rangle k_u \{V_j\}}{\partial x_j} = \mathcal{P}_{b_u} + \mathcal{P}_{s_u} - \mathcal{E}_u + \frac{\partial}{\partial x_j}\left(\frac{\langle\rho\rangle \nu_u}{\sigma_k}\frac{f_\varepsilon}{f_k^2}\frac{\partial k_u}{\partial x_j}\right), \tag{48}$$

where

$$\mathcal{E}_u = \langle\rho\rangle \varepsilon_u = \langle\rho\rangle \frac{k_u^{3/2}}{S_u}. \tag{49}$$

We recall that the derivation of Eq. (48) assumes that f_k and f_ε are constant. If this property does not hold, the model's derivation needs to consider additional terms [33] and the modeled-to-total ratio of density, f_ρ. Despite being commonly neglected, this requirement holds for any bridging and hybrid formulation.

2. S_u evolution equation

The derivation of the evolution equation for S_u is similar to that for k_u. From f_S, it is possible to establish the following relationship between the evolution equations for S_u (PANS) and S_t (RANS):

$$\frac{\partial \overline{\rho} S_u}{\partial t} + \frac{\partial \overline{\rho} S_u \tilde{V}_j}{\partial x_j} = f_S\left[\frac{\partial \overline{\rho} S_t}{\partial t} + \frac{\partial \overline{\rho} S_t \tilde{V}_j}{\partial x_j}\right], \tag{50}$$

which can be rewritten as

$$\frac{\partial \langle\rho\rangle S_u}{\partial t} + \frac{\partial \langle\rho\rangle S_u \{V_j\}}{\partial x_j} \approx f_\rho f_S\left[\frac{\partial \overline{\rho} S_t}{\partial t} + \frac{\partial \overline{\rho} S_t \tilde{V}_j}{\partial x_j}\right], \tag{51}$$

using the zero transport model [27]. Now, we replace the material derivative of S_t by the right-hand side of Eq. (25),

$$\frac{\partial \langle\rho\rangle S_u}{\partial t} + \frac{\partial \langle\rho\rangle S_u \{V_j\}}{\partial x_j} = f_\rho f_S \frac{S_t}{k_t}\left(c_4 \mathcal{P}_{b_t} + c_1 \mathcal{P}_{s_t}\right) - f_\rho f_S c_2 \overline{\rho}\sqrt{k_t} + f_\rho f_S \frac{\partial}{\partial x_j}\left(\frac{\overline{\rho}\nu_t}{\sigma_S}\frac{\partial S_t}{\partial x_j}\right). \tag{52}$$

Using the parameters f_k and f_ε, the definition of f_S, and relationships (43) and (44), we obtain

$$\begin{aligned}\frac{\partial \langle\rho\rangle S_u}{\partial t} + \frac{\partial \langle\rho\rangle S_u \{V_j\}}{\partial x_j} = {} & \frac{\partial}{\partial x_j}\left(\frac{\langle\rho\rangle \nu_u}{\sigma_S}\frac{f_\varepsilon}{f_k^2}\frac{\partial S_u}{\partial x_j}\right) - c_2 \frac{f_k}{f_\varepsilon}\langle\rho\rangle\sqrt{k_u} \\ & + \frac{S_u}{k_u} c_4 f_k\left(\frac{\mathcal{P}_{b_u}}{f_k} - \omega_b \langle\rho\rangle \frac{k_u^{3/2}}{S_u}\left[\frac{1}{f_k} - \frac{1}{f_\varepsilon}\right]\right) \\ & + \frac{S_u}{k_u} c_1 f_k\left(\frac{\mathcal{P}_{s_u}}{f_k} - \omega_s \langle\rho\rangle \frac{k_u^{3/2}}{S_u}\left[\frac{1}{f_k} - \frac{1}{f_\varepsilon}\right]\right).\end{aligned} \tag{53}$$

This equation can be rearranged by introducing the coefficient c_2^*,

$$\frac{\partial \langle\rho\rangle S_u}{\partial t} + \frac{\partial \langle\rho\rangle S_u \{V_j\}}{\partial x_j} = \frac{\partial}{\partial x_j}\left(\frac{\langle\rho\rangle \nu_u}{\sigma_S}\frac{f_\varepsilon}{f_k^2}\frac{\partial S_u}{\partial x_j}\right) - c_2^* \langle\rho\rangle\sqrt{k_u} + \frac{S_u}{k_u}\left(c_4 \mathcal{P}_{b_u} + c_1 \mathcal{P}_{s_u}\right), \tag{54}$$

$$c_2^* = c_2 \frac{f_k}{f_\varepsilon} + (c_4 \omega_b + c_1 \omega_s)\left(1 - \frac{f_k}{f_\varepsilon}\right). \tag{55}$$

3. a_{u_i} evolution equation

The production terms of k_u and S_u in PANS BHR-LEVM closure require the calculation of the velocity mass flux, a_i, which is obtained from an additional evolution equation. The derivation of the PANS equation for a_i starts by establishing the following relationship:

$$\frac{\partial \overline{\rho} a_{i_u}}{\partial t} + \frac{\partial \overline{\rho} a_{i_u} \tilde{V}_j}{\partial x_j} = f_{a_i}\left[\frac{\partial \overline{\rho} a_{i_t}}{\partial t} + \frac{\partial \overline{\rho} a_{i_t} \tilde{V}_j}{\partial x_j}\right]. \tag{56}$$

Following the approach used for the k_u and S_u equations, the left-hand side of Eq. (56) can be approximated as

$$\frac{\partial \langle\rho\rangle a_{i_u}}{\partial t} + \frac{\partial \langle\rho\rangle a_{i_u}\{V_j\}}{\partial x_j} \approx f_\rho f_{a_i}\left[\frac{\partial \overline{\rho} a_{i_t}}{\partial t} + \frac{\partial \overline{\rho} a_{i_t} \tilde{V}_j}{\partial x_j}\right], \tag{57}$$

using the zero transport model [27]. Next, we replace the right-hand side of this equation by that of Eq. (26),

$$\begin{aligned}\frac{\partial \langle\rho\rangle a_{i_u}}{\partial t} + \frac{\partial \langle\rho\rangle a_{i_u}\{V_j\}}{\partial x_j} = f_\rho f_{a_i}\Bigg[&b_t \frac{\partial \overline{P}}{\partial x_i} + R^1(V_i, V_j)\frac{\partial \overline{\rho}}{\partial x_j} - \overline{\rho} a_{j_t}\frac{\partial \overline{V}_i}{\partial x_j} + \overline{\rho}\frac{\partial (a_{i_t} a_{j_t})}{\partial x_j} \\ &- c_{a_1}\overline{\rho} a_{i_t}\frac{\sqrt{k_t}}{S_t} + \frac{\partial}{\partial x_j}\left(\frac{\overline{\rho}\nu_t}{\sigma_a}\frac{\partial a_{i_t}}{\partial x_j}\right)\Bigg].\end{aligned} \tag{58}$$

The final step to derive the a_{u_i} equation is to express the right-hand side of Eq. (58) in terms of filtered and unresolved quantities. This can be accomplished through the parameters f_k, f_ε, f_{a_i}, f_b, and key closure simplifications,

$$f_\rho f_{a_i} b_t \frac{\partial \overline{P}}{\partial x_i} \approx f_{a_i}\frac{b_u}{f_b}\frac{\partial \langle P\rangle}{\partial x_i}, \tag{59}$$

$$f_\rho f_{a_i} R^1(V_i, V_j)\frac{\partial \overline{\rho}}{\partial x_j} \approx \frac{f_{a_i}}{f_k}\tau^1(V_i, V_j)\frac{\partial \langle\rho\rangle}{\partial x_j}, \tag{60}$$

$$\begin{aligned} f_\rho f_{a_i}\overline{\rho} a_{j_t}\frac{\partial \overline{V}_i}{\partial x_j} &= \frac{f_{a_i}}{f_{a_j}}\langle\rho\rangle a_{j_u}\frac{\partial \overline{V}_i}{\partial x_j} \\ &= \frac{f_{a_i}}{f_{a_j}}\langle\rho\rangle a_{j_u}\left[\frac{\partial \langle V_i\rangle}{\partial x_j} + \left(\frac{\partial \overline{V}_i}{\partial x_j} - \frac{\partial \langle V_i\rangle}{\partial x_j}\right)\right] \\ &= \frac{f_{a_i}}{f_{a_j}}\langle\rho\rangle a_{j_u}\frac{\partial \langle V_i\rangle}{\partial x_j} \quad \text{(ZTM)},\end{aligned} \tag{61}$$

$$f_\rho f_{a_i}\overline{\rho}\frac{\partial (a_{i_t} a_{j_t})}{\partial x_j} = \frac{\langle\rho\rangle}{f_{a_j}}\frac{\partial (a_{i_u} a_{j_u})}{\partial x_j}, \tag{62}$$

$$f_\rho f_{a_i} c_{a_1}\overline{\rho} a_{i_t}\frac{\sqrt{k_t}}{S_t} = c_{a_1}\langle\rho\rangle a_{i_u}\frac{\sqrt{k_u}}{S_u}\frac{f_k}{f_\varepsilon}, \tag{63}$$

$$f_\rho f_{a_i}\frac{\partial}{\partial x_j}\left(\frac{\overline{\rho}\nu_t}{\sigma_a}\frac{\partial a_{i_t}}{\partial x_j}\right) = \frac{\partial}{\partial x_j}\left(\frac{\langle\rho\rangle\nu_u}{\sigma_a}\frac{f_\varepsilon}{f_k^2}\frac{\partial a_{i_u}}{\partial x_j}\right). \tag{64}$$

These six terms allow us to rearrange Eq. (58) and obtain its final form,

$$\begin{aligned}\frac{\partial \langle\rho\rangle a_{i_u}}{\partial t} + \frac{\partial \langle\rho\rangle a_{i_u}\{V_j\}}{\partial x_j} = &f_{a_i}\frac{b_u}{f_b}\frac{\partial \langle P\rangle}{\partial x_i} + \frac{f_{a_i}}{f_k}\tau^1(V_i, V_j)\frac{\partial \langle\rho\rangle}{\partial x_j} - \frac{f_{a_i}}{f_{a_j}}\langle\rho\rangle a_{j_u}\frac{\partial \langle V_i\rangle}{\partial x_j} + \frac{\langle\rho\rangle}{f_{a_j}}\frac{\partial (a_{i_u} a_{j_u})}{\partial x_j} \\ &- c_{a_1}\langle\rho\rangle a_{i_u}\frac{\sqrt{k_u}}{S_u}\frac{f_k}{f_\varepsilon} + \frac{\partial}{\partial x_j}\left(\frac{\langle\rho\rangle\nu_u}{\sigma_a}\frac{f_\varepsilon}{f_k^2}\frac{\partial a_{i_u}}{\partial x_j}\right).\end{aligned} \tag{65}$$

4. b_u evolution equation

The derivation of PANS BHR-LEVM closure concludes with the evolution equation for the unresolved density-specific volume correlation, b_u. Once again, we start by establishing the following relationship using the parameter f_b:

$$\frac{\partial \overline{\rho} b_u}{\partial t} + \frac{\partial \overline{\rho} b_u \tilde{V}_j}{\partial x_j} = f_b \left[\frac{\partial \overline{\rho} b_t}{\partial t} + \frac{\partial \overline{\rho} b_t \tilde{V}_j}{\partial x_j} \right], \tag{66}$$

which, using the ZTM model [27], can be simplified as follows:

$$\frac{\partial \langle\rho\rangle b_u}{\partial t} + \frac{\partial \langle\rho\rangle b_u \{V_j\}}{\partial x_j} \approx f_\rho f_b \left[\frac{\partial \overline{\rho} b_t}{\partial t} + \frac{\partial \overline{\rho} b_t \tilde{V}_j}{\partial x_j} \right]. \tag{67}$$

Replacing the term between brackets by the right-hand side of Eq. (27),

$$\frac{\partial \langle\rho\rangle b_u}{\partial t} + \frac{\partial \langle\rho\rangle b_u \{V_j\}}{\partial x_j} = f_\rho f_b \left[2\overline{\rho} a_{j_t} \frac{\partial b_t}{\partial x_j} - 2a_{j_t}(b_t + 1)\frac{\partial \overline{\rho}}{\partial x_j} - c_b \overline{\rho} b_t \frac{\sqrt{k_t}}{S_t} + f_b \overline{\rho}^2 \frac{\partial}{\partial x_j}\left(\frac{\nu_t}{\overline{\rho}\sigma_b} \frac{\partial b_t}{\partial x_j} \right) \right], \tag{68}$$

and converting total to partial quantities using f_ϕ, we get the final form of the b_u equation,

$$\begin{aligned} \frac{\partial \langle\rho\rangle b_u}{\partial t} + \frac{\partial \langle\rho\rangle b_u \{V_j\}}{\partial x_j} &= 2\langle\rho\rangle \frac{a_{j_u}}{f_{a_j}} \frac{\partial b_u}{\partial x_j} - 2\frac{a_{j_u}}{f_{a_j}}(b_u + f_b)\frac{\partial \langle\rho\rangle}{\partial x_j} - c_b \langle\rho\rangle b_u \frac{f_k}{f_\varepsilon}\frac{\sqrt{k_u}}{S_u} \\ &\quad + \langle\rho\rangle^2 \frac{\partial}{\partial x_j}\left(\frac{\nu_u}{\langle\rho\rangle\sigma_b} \frac{f_\varepsilon}{f_k^2} \frac{\partial b_u}{\partial x_j} \right). \end{aligned} \tag{69}$$

Thus, the PANS BHR-LEVM closure is composed by Eqs. (48), (54), (65), and (69). Note that the PANS BHR-LEVM closure recovers its original RANS form when all f_ϕ are equal to unity.

III. FILTER CONTROL PARAMETER

The efficiency of bridging and hybrid formulations is determined by the degree of physical resolution. As the model resolves a wider range of flow scales, both the cost and accuracy of the simulations are expected to grow. Whereas excessive physical resolution reduces the computational efficiency by increasing the cost without commensurate improvement in accuracy, insufficient resolution can compromise accuracy by precluding the model from resolving the scales not amenable to modeling [22,40,49,50]. Hence, the success of such SRS methods is dictated by the parameters controlling their physical resolution.

As discussed in [40], there are three main factors to consider when determining the physical resolution needed for a given model, flow configuration, and quantities of interest:

(i) The length- and timescales that need to be resolved.

(ii) The smallest flow scales that the selected spatiotemporal grid resolution and numerical setup can accurately resolve.

(iii) The effect of the physical resolution on the dependent variables of the turbulence closure.

The authors have recently investigated the first point through the analysis of flows around cylinders and the Taylor-Green vortex [22,40,49,50]. These studies have shown that the accurate prediction of these complex problems is determined by the mathematical model's ability to resolve the instabilities and coherent structures governing the flow physics. This flow physics is dominated by nonlocal effects, which most one-point closures cannot represent accurately. Thus, accurate computations of such problems require resolving the Kelvin-Helmholtz rollers observed in flows past cylinders in the subcritical regime [51,52], and the vortex-reconnection process of the TGV. The remaining flow scales can be accurately modeled through an adequate turbulence closure model. These studies also illustrate the importance of understanding the flow physics and its main features to select the physical resolution and obtain high-fidelity solutions.

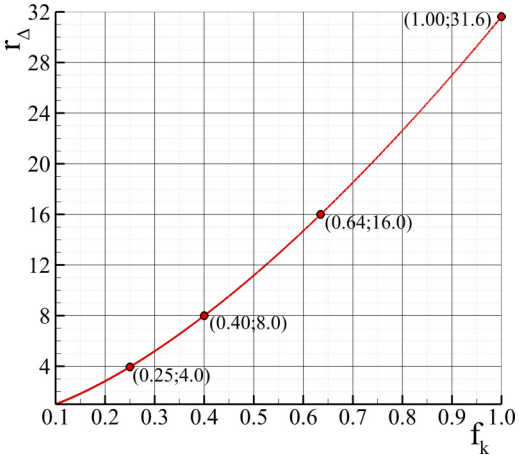

FIG. 1. Ratio between the minimum spatial grid resolution needed for computations at a given f_k and $(f_k)_{\text{ref}} = 0.10$, r_Δ [40].

The second aspect is ideally addressed through verification exercises [38,39,53]. We have illustrated the crucial role of verification of RANS and SRS predictions in [40,45,50,54,55]. It is possible to obtain a reasonable *a priori* estimate of the maximum physical resolution that a given grid can support and, conversely, the dependency of the grid requirements from the physical resolution. Irrespective of the numerical scheme, using Kolmogorov arguments, and assuming high-Re flow ($f_\varepsilon = 1.0$), it is possible to obtain an expression to estimate the smallest value of f_k that a spatial grid resolution can accurately resolve [40],

$$f_k \geqslant \left(\frac{1}{c_\mu}\right)^{1/2} \left(\frac{\Delta}{k_t^{1.5}/\varepsilon_t}\right)^{2/3}. \tag{70}$$

This expression can be rearranged to provide the ratio between the smallest grid size for two values of f_k,

$$r_\Delta = \frac{\Delta_{f_k}}{\Delta_{(f_k)_{\text{ref}}}} = \left(\frac{f_k}{(f_k)_{\text{ref}}}\right)^{3/2}, \tag{71}$$

where Δ is the grid resolution or size, and the subscript "ref" denotes a reference f_k ($f_{k_{\text{ref}}} > 0$). This expression enables the evaluation of the relative evolution of Δ with the physical resolution. Note that it is possible to use different arguments and expressions to perform this simple, *a priori*, and qualitative assessment of the impact of f_k on the grid requirements of the model.

Figure 1 depicts the evolution of Δ with f_k relative to the case $(f_k)_{\text{ref}} = 0.10$. The results show the close dependence between the grid and physical (f_k) resolutions. As f_k increases, the minimum grid resolution coarsens as $(10 f_k)^{1.5}$. Considering the cases of $f_k = 0.25$ and 0.40, this represents reducing the grid resolution requirements by a factor of 4 and 8 when compared to the case at $f_k = 0.10$. Since SRS computations are inherently three-dimensional and unsteady, Fig. 1 confirms the potential of bridging methods to predict complex flows efficiently. It also emphasizes the importance of selecting an adequate physical resolution for a given problem and quantities of interest.

The third factor is caused by the fact that an SRS model's physical resolution does not affect all turbulence-dependent quantities equally, i.e., a given range of resolved scales does not lead to equal ratios modeled-to-total for all dependent variables of the closure model. For instance, it is not expected that the turbulence kinetic energy and dissipation possess similar spectral signatures in a fully developed turbulent flow [56,57]. This has been recently addressed in Pereira *et al.* [40]. We

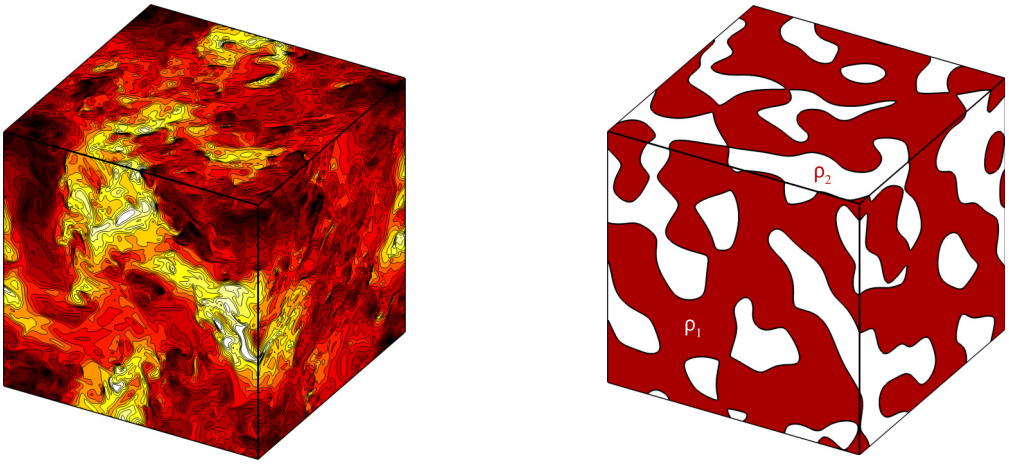

(a) FHIT - $V_1(\mathbf{x})$ (b) HVDT - $\rho(\mathbf{x}, t_o)$

FIG. 2. FHIT and HVDT DNS velocity and density ($t = 0$) flow fields.

emphasize that despite most SRS models neglecting this aspect, PANS can consider the spectral signature of each dependent quantity of the closure through f_ϕ. This benefit comes at the expense of having to determine the other control parameters in such a manner that consistency between the various physical processes can be preserved.

The PANS BHR-LEVM model relies on f_k, f_ε, f_{a_i}, and f_b to set the physical resolution. The parameter f_k can be either set constant [27,54,58,59] or dynamically [58,60–62] in space and time. Although the second approach may enhance the simulation's efficiency, we choose using constant values of f_k to prevent commutation errors [32,33] and enable robust verification and validation exercises where one can evaluate numerical and modeling errors separately to avoid possible error canceling [63]. Regarding f_ε, this parameter is commonly defined constant and equal to 1. This modeling assumption stems from the fact that most turbulence dissipation in high-Re flows occurs at the smallest scales [56,57]. For this reason, $f_\varepsilon = 1.00$ is often used in practical PANS simulations. The validity of this option has been recently confirmed by the authors [40], and it is discussed in Sec. III A 1. The remaining parameters, f_{a_i} and f_b, have never been used before and so their definition needs to be investigated; see Sec. III A 2.

The remainder of this section addresses the specification of the parameters f_ϕ in PANS BHR-LEVM, in a manner that is consistent with the implicit-filter corresponding to f_k. Unfortunately, canonical turbulence theories cannot be used for this purpose. Instead, this objective is accomplished through *a priori* testing, in which the parameters f_ϕ are calculated at successively smaller physical resolutions—from $f_k = 0.00$ to 1.00. The selected canonical flows are the forced homogeneous isotropic turbulence (FHIT) of Silva *et al.* [64] at Taylor Reynolds numbers $\mathrm{Re}_\lambda = 140$ and 300, and the buoyancy-driven homogeneous variable-density turbulence (HVDT [65–68]) of Aslangil *et al.* [69,70] at $\mathrm{At} = 0.75$. These flow problems have been simulated by means of DNS in a cubical domain of length 2π, and their streamwise velocity (FHIT) and density (HVDT) fields are depicted in Fig. 2. All computations were performed in a 1024^3 mesh, except the FHIT at $\mathrm{Re}_\lambda = 140$, which used a 512^3 grid. The comprehensive description of these data sets is given in [64,67–70].

The ratios modeled-to-total, f_ϕ, of the dependent quantities of PANS BHR-LEVM at a distinct filter's cutoff are computed as follows. The DNS flow fields are filtered using the operator [71,72]

$$\langle \Phi \rangle(\mathbf{x}) = \int_{-\Delta/2}^{+\Delta/2} \int_{-\Delta/2}^{+\Delta/2} \int_{-\Delta/2}^{+\Delta/2} \Phi(\mathbf{x})\, G_\Delta(\mathbf{x} - \mathbf{x}') d\mathbf{x}', \tag{72}$$

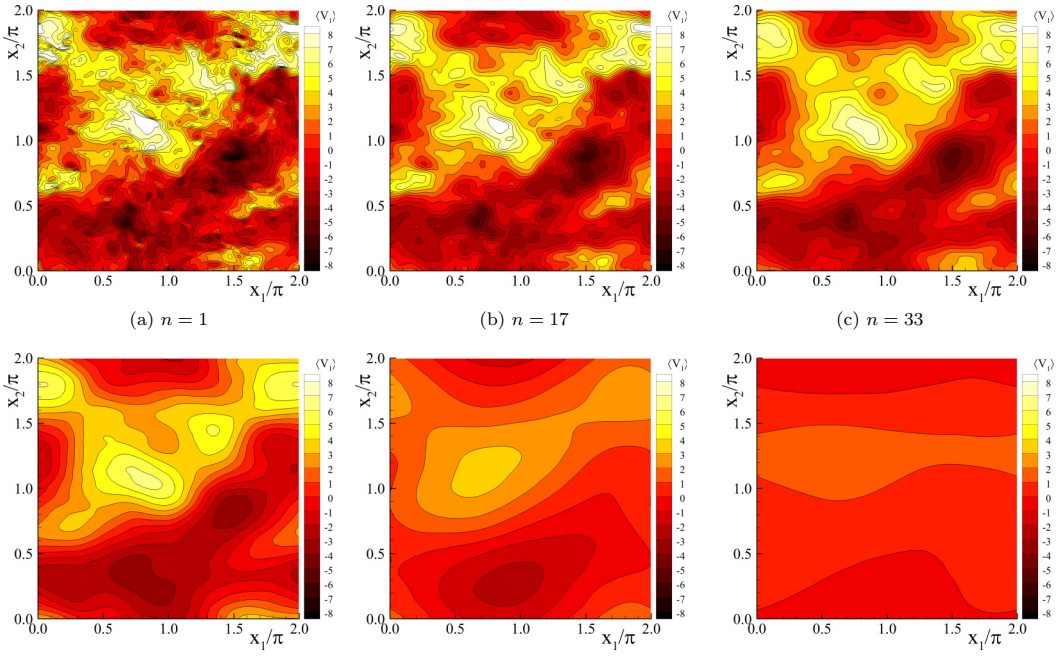

FIG. 3. Evolution of x_1-component of the FHIT velocity field with the relative filter length size, $n = \Delta/\Delta_\eta$.

where bold symbols denote vectors, Δ is the filter's width, and G_Δ is the kernel of the filtering operator. Here, we use a box filter so that

$$G_\Delta(\mathbf{x} - \mathbf{x}') = \begin{cases} \Delta^{-1}, & |\mathbf{x} - \mathbf{x}'| < 0.5\Delta, \\ 0 & \text{otherwise.} \end{cases} \tag{73}$$

Figure 3 illustrates the effect of varying this operator filter's width on the velocity field of the FHIT flow. As the filter's width increases, the magnitude of the filtered turbulent velocity field asymptotes to zero, and its gradients get smoother. This is the reasoning for the cost reduction observed from DNS to RANS [45]. It is important to note that the shape of the filter implied by the PANS decomposition is not known, however the utilization of a box filter is not expected to alter the conclusions of this class of studies [73–75] (see Sec. III A 2 for HVDT). This idea is confirmed by comparing our HVDT results with those of Saenz *et al.* [76] obtained with a Gaussian filter. Both studies lead to similar qualitative conclusions. In contrast, cutoff filters are not suitable for this exercise since practical SRS computations do not rely on such operators [73,77]. It is also generally accepted that the box filtering operator is the closest approach to the implicit filtering of finite-difference and finite-volume discretization schemes utilized in engineering computations [72,78,79]. For all these reasons, the use of a box filter operator is not expected to affect the qualitative conclusions of the present analysis.

For any given filter $\{\cdot\}$ or $\langle\cdot\rangle$ chosen, the unresolved dependent variables of the BHR-LEVM closure are calculated from relations (14) and (15) [19,34,80],

$$k_u = 0.5(\{V_i V_i\} - \{V_i\}\{V_i\}), \tag{74}$$

$$\varepsilon_u = \nu\left(\left\{\frac{\partial V_i}{\partial x_j}\frac{\partial V_i}{\partial x_j}\right\} - \left\{\frac{\partial V_i}{\partial x_j}\right\}\left\{\frac{\partial V_i}{\partial x_j}\right\}\right), \tag{75}$$

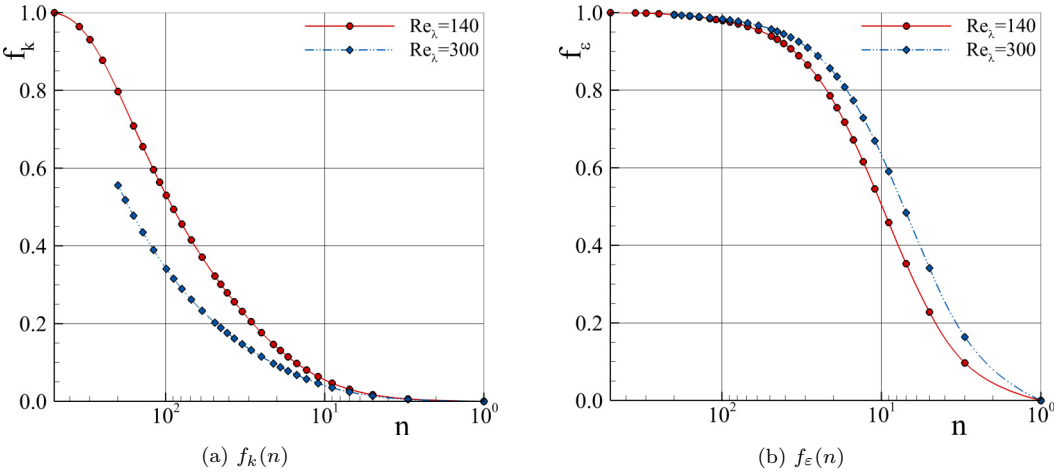

FIG. 4. Variation of f_k and f_ε with the relative filter size, n, at $\mathrm{Re}_\lambda = 140$ and 300.

$$a_{i_u} = \frac{\langle \rho' v_i' \rangle - \langle \rho' \rangle \langle v_i' \rangle}{\langle \rho \rangle}, \tag{76}$$

$$b_u = \langle \rho' \rangle \langle (1/\rho)' \rangle - 1. \tag{77}$$

It is crucial to emphasize that ρ' and v_i' in Eqs. (76) and (77) consider the fluctuating component of the density and velocity fields, i.e., these quantities can comprise both the coherent and stochastic fields [17,18]. Yet, the stochastic field is expected to be the main contributor to a_{u_i} and b_u at late times when the flow exhibits fully developed and high-intensity turbulence features. The quantities given by relations (74)–(77) are calculated with $n = \Delta/\Delta_\eta$ up to 349, where Δ_η is the grid size used in the DNS simulations. Note that due to the objective and computational cost of these exercises, only the FHIT case at $\mathrm{Re}_\lambda = 140$ is filtered until $f_k \approx 1$. This study is performed with the code used in [45,55].

The outcome of the *a priori* exercises is now discussed in Sec. III A. However, before presenting the results, note that the FHIT problem is an archetypal problem widely utilized to investigate the dynamics and modeling of fully developed incompressible turbulence. For this reason, we use this flow to analyze the dependence of f_k and f_ε on the range of resolved scales [40]. On the other hand, the HVDT flow is a canonical problem used to study the fundamental physics and modeling of variable-density flow. Hence, we use the HVDT case to investigate the evolution of f_k, f_{a_i}, and f_b with the physical resolution.

A. *A priori* testing results

1. Forced homogeneous isotropic turbulence

Figure 4 presents the variation of f_k and f_ε with the relative filter size, $n = \Delta/\Delta_\eta$. n indicates how large the filter size is when compared to DNS resolution (so $n = 1$ is DNS). As expected, the $f_k(n)$ results indicate that most turbulence kinetic energy is contained at the largest flow scales. This behavior gets more pronounced with increasing Re_λ. It is observed that to filter only 20% of the total turbulence kinetic energy, we need $n = 29$ ($\mathrm{Re}_\lambda = 140$) and 49 ($\mathrm{Re}_\lambda = 300$). This clearly illustrates the potential of bridging models to efficiently compute complex flow problems. Also, note that bridging models are usually not used at $f_k < 0.20$ (LES range [56]). Regarding f_ε, the results of Fig. 4 confirm that most turbulence dissipation occurs at the smallest scales and, as such,

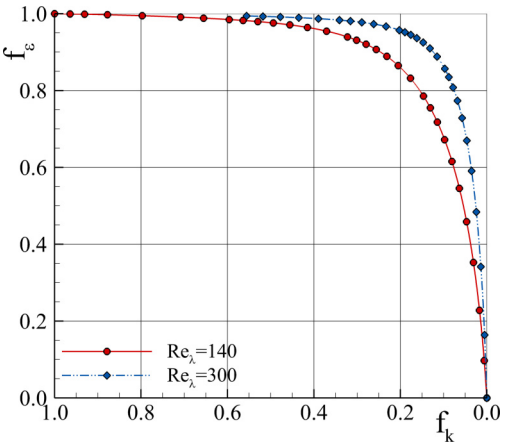

FIG. 5. f_ε as a function of f_k at $\mathrm{Re}_\lambda = 140$ and 300.

f_ε grows significantly more rapidly than f_k with n. The data show $f_\varepsilon = 0.22$ ($\mathrm{Re}_\lambda = 140$) and 0.34 ($\mathrm{Re}_\lambda = 300$) for $n = 5$, and $f_\varepsilon > 0.99$ for $n = 199$ and both Reynolds numbers.

Next, Fig. 5 presents f_ε as a function of f_k. The results indicate that f_ε is only weakly dependent on f_k at coarser f_k values. At $f_k = 0.20$, $f_\varepsilon = 0.87$ for $\mathrm{Re}_\lambda = 140$ and $f_\varepsilon = 0.93$ for $\mathrm{Re}_\lambda = 300$. Considering that practical simulations of turbulence are expected to operate at $f_k \geqslant 0.20$ due to the inherent cost and availability of LES formulations, Fig. 5 confirms that $f_\varepsilon = 1.00$ is a good assumption for practical PANS computations.

2. Homogeneous variable-density turbulence

The HVDT is a transient flow and, as such, the *a priori* tests are conducted at the three distinct and representative times shown in Fig. 6: at $t_1 = 1.8$, the flow is in the so-called explosive growth regime [70] and the kinetic energy of the system is rapidly increasing through the conversion of potential into kinetic energy. As shown in Fig. 6(a), the flow does not exhibit small-scale turbulence, and the two fluids ($\rho_1 = 7.0$ and $\rho_2 = 1.0$) are mostly unmixed. At $t_2 = 2.8$, the flow kinetic energy grows, reaching close to its peak. This leads to flow regions characterized by small-scale turbulence, where the two fluids mix. Finally, $t_3 = 4.8$ is just after the fast decay regime where the kinetic energy decays rapidly. Turbulence is the major component of the kinetic energy, and the flow exhibits high-intensity and fully developed turbulence features. This enhances mixing [compare Figs. 6(b) and 6(c)]. A comprehensive description of this flow is given in Aslangil *et al.* [69,70]. It is important to emphasize that the transient nature of the HVDT flow and the overlap between coherent and turbulent wavelengths/frequencies hamper *a priori* exercises of this class of flows. Nonetheless, these studies still provide valuable information about the flow physics and evolution f_ϕ with the filter size.

Figures 7 and 8 present the variation of f_k, f_a, and f_b with the relative filter size, and the energy spectra of k_t, a_t, and b_t for the unfiltered fields. Due to the HVDT flow properties, the quantities $\overline{a}_2$ and $\overline{a}_3$ are equal to zero, so we consider $f_a = f_{a_1}$. The results for $f_k(n)$ indicate that before the peak of k_t ($t = t_1$), most of the kinetic energy is contained in the largest coherent flow scales (blobs of laminar fluid). For this reason, f_k does not exceed 0.38 when $n = 99$. As the flow and turbulence field develop, $t = t_2$, k_t increases to a value close to its maximum, altering the spectral properties of the kinetic energy field. In addition to the conversion of potential into kinetic energy, the energy of the largest scales is transferred to the smallest ones, widening the spectra so that larger fractions of k_t are modeled for the same n. At later times, $t = t_3$, when the flow exhibits high-intensity turbulence

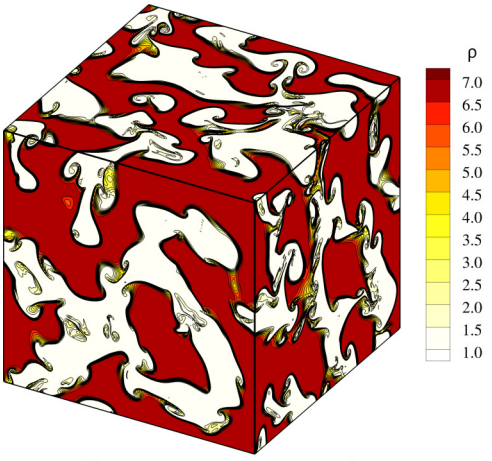

(a) $t = t_1$

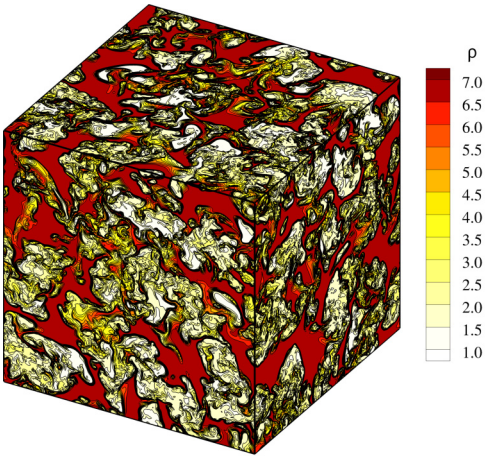

(b) $t = t_2$

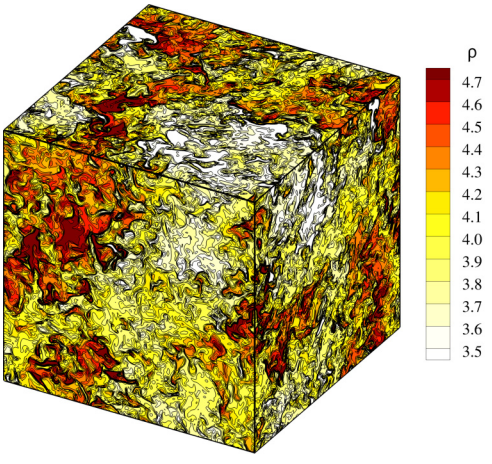

(c) $t = t_3$

FIG. 6. Density field of HVDT flow at distinct times: before (t_1), at (t_2), and after (t_3) the peak of kinetic energy.

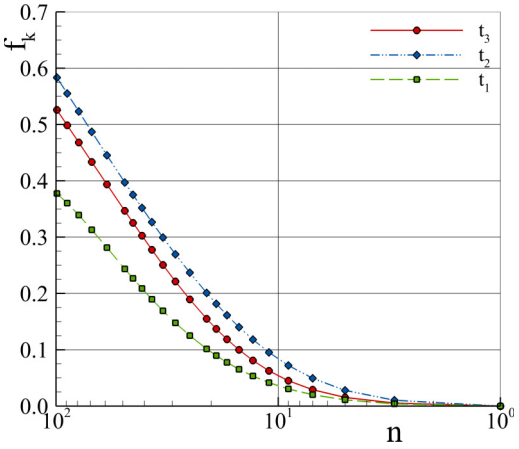

(a) $f_k(n)$

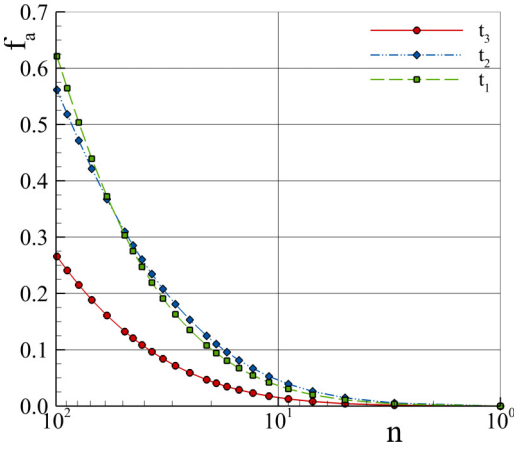

(b) $f_a(n)$

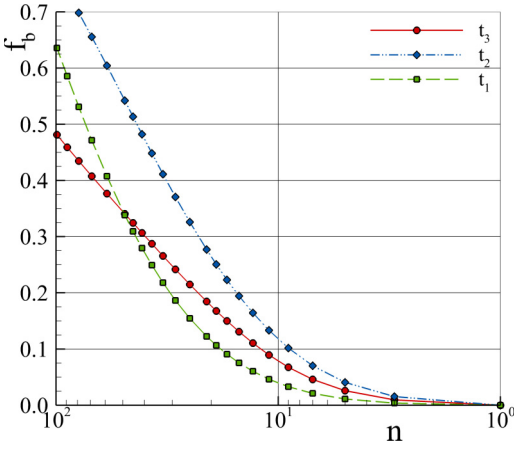

(c) $f_b(n)$

FIG. 7. Variation of f_k, f_a, and f_b with the relative filter size, n, at distinct times.

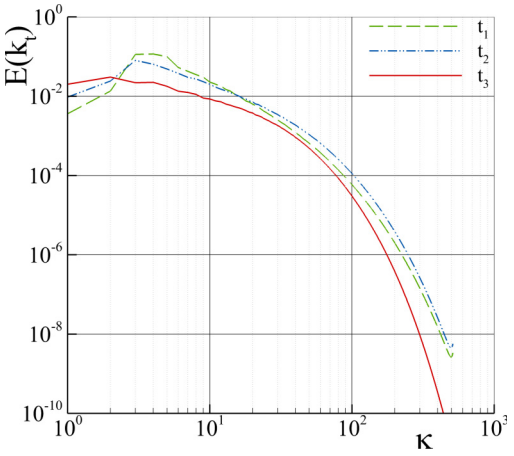

(a) $E(k)$

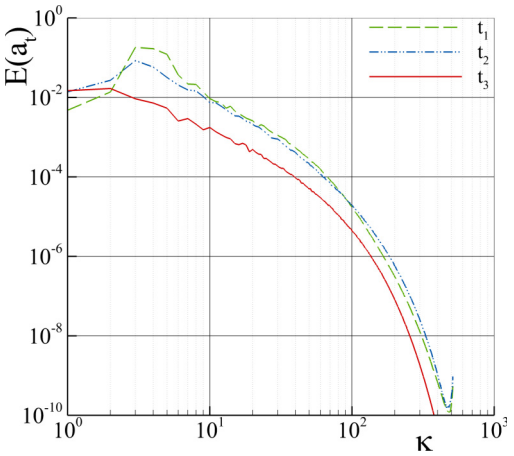

(b) $E(a)$

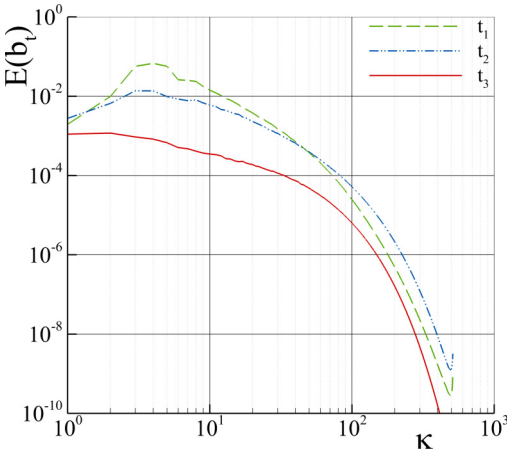

(c) $E(b)$

FIG. 8. Energy spectra of k_t, a_t, and b_t at distinct times.

and mixing, $f_k(n)$ exhibits a slight reduction. This stems from the dissipation of k_t at the smallest scales.

Turning our attention to $f_a(n)$, the results indicate that the evolution of this quantity with the filter width at $t = t_1$ and t_2 is nearly identical. This shows that the morphological flow changes occurring at these early instants significantly affect the turbulence kinetic energy but not the velocity fluctuations uncorrelated with the density field [Figs. 8(b) and 8(c)]. The data of Fig. 7(b) also indicate that approximately 60% of the energy of a at these instants is contained in the smallest flow scales, $n = 99$. At $t = t_3$, the values of f_a are reduced approximately 50% . Note that this is when the flow exhibits high-intensity turbulence, a more homogeneous mixture, and diminishing influence of the coherent field (Fig. 7).

The variation of f_b with n shows that the magnitude of this quantity increases from $t = t_1$ to t_2, reaching values of 0.63 at $t = t_1$ and 0.77 at t_2. Such results indicate that the density-specific volume correlation is dominated by the smallest wavelengths at these early stages. The observed high-intensity turbulence and enhanced mixing at $t = t_3$ leads to a significant reduction of f_b. For $n \leqslant 99$, f_b does not exceed 0.50.

As for the FHIT case, Fig. 7 illustrates the potential of bridging models to compute complex flow problems efficiently. Considering f_k, the data indicate that simulations at $f_k = 0.50$ and 0.25 ($t = t_3$) can run on grid resolutions 89 and 33 times coarser (in each direction) than those required by DNS. This constitutes a significant cost reduction.

Finally, Fig. 9 depicts the variation of f_a and f_b as a function of f_k. The results show that the ratio f_a/f_k gets smaller in time, and $f_a \approx f_k/2$ at $t = t_3$ (the instant when the flow is characterized by high-intensity turbulence). In contrast, f_b has a small temporal dependence until t_2, and $f_b > f_k$. Such a behavior is not observed at $t = t_3$, where $f_b \approx f_k$. We attribute this result to the breakdown into turbulence and dissipation of the coherent field.

3. Parameter selection

The above *a priori* tests have been conducted to help us determine the parameters f_ϕ of PANS BHR-LEVM, and to propose guidelines toward their efficient selection. Nevertheless, we reiterate that the present paper's primary objectives are to extend PANS methodology to variable-density flow and provide the resulting PANS BHR-LEVM model's initial validation space. Closures using different dependent variables may require similar studies to define f_ϕ (only k and ε tend to be used in most closures [14,81,82]).

The FHIT results have shown that prescribing $f_\varepsilon = 1.00$ is a good strategy because most dissipation occurs at the smallest flow scales. These are usually modeled in practical PANS computations ($f_k \geqslant 0.20$). Although f_k and f_ε can get closer in transient and/or transitional flows, the results available in the extensive PANS literature have shown that this approach is still good [27,40,48,49,54,58,59,61,83–85]. In these cases, the resulting modeling shortcomings need to be compensated by slighter finer values of f_k. Referring to f_a and f_b, selecting these parameters is more complex and has never been done before. Our *a priori* tests suggest setting $f_a = f_k/2$ and $f_b = f_k$ at late times when turbulence is closer to fully developed, and the coherent field has a diminishing impact on the flow dynamics. However, note that these quantities are inherently time-dependent and contain a meaningful coherent component at early times. Once again, these calibration issues can be overcome through a proper selection of f_ϕ, and slightly lower values of f_k. Although often neglected, it is crucial to emphasize that these issues are common to most SRS models.

Considering the previous points and the results of the *a priori* tests, the present simulations utilize one of the following strategies to define f_k, f_ε, f_a ($f_a = f_{a_i}$), and f_b:

(i) Upon inspection of the governing equations of the PANS BHR-LEVM closure, it is possible to infer that f_k and f_ε are the major influence on the production of modeled turbulent kinetic energy by shear and buoyancy effects (k_u and S_u equations), and, consequently, on the modeled turbulent stresses. Thus, we prescribe f_k, define $f_\varepsilon = 1.00$ based on the outcome of the *a priori* exercises, and

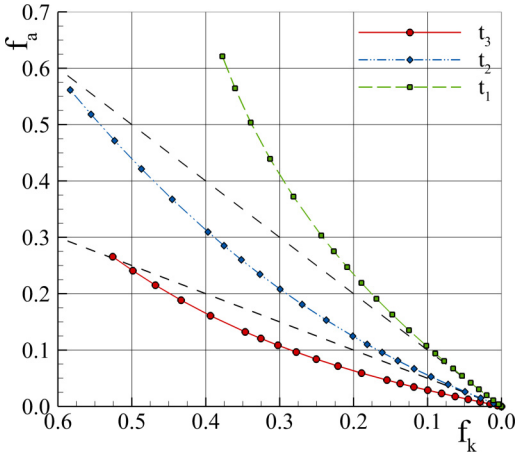

(a) $f_a(f_k)$

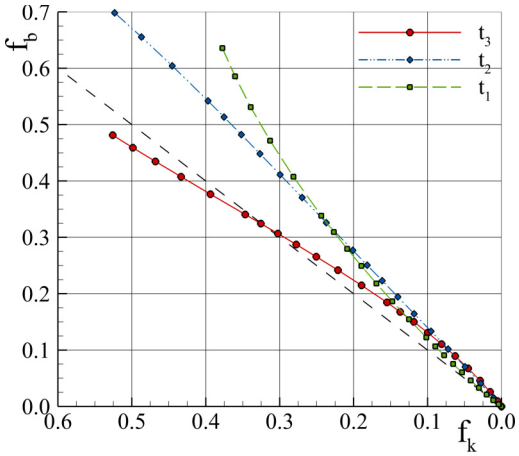

(b) $f_b(f_k)$

FIG. 9. Variation of f_a and f_b with f_k at distinct times.

set the remaining parameters equal to 1. We expect this approach to be more robust and general so it can be applied to most flows. Yet, it might require slightly smaller values of f_k to compensate for possible calibration deficits.

(ii) Disregard the contribution of the density fluctuations to the specification of f_a and f_b [Eqs. (20), (21), and (30)] by assuming that the coherent field is the main contributor to the magnitude of a_{i_u} and b_u. This makes f_a only dependent on the velocity field so that $f_a \approx \sqrt{f_k}$ and $f_b \approx 1.00$. f_ε is set equal to 1 based on the *a priori* results.

(iii) Based on the outcome of the *a priori* exercises of the FHIT and HVDT, set $f_a \approx f_k/2$, $f_\varepsilon = 1.00$, and $f_b \approx f_k$. This strategy is optimized for the HVDT type of flows, and best suited for instants characterized by fully developed turbulence.

These approaches are summarized in Table II and tested in Sec. V B. Note that for S_3, the values of f_a are rounded to the closest upper multiple of 0.05. In the remainder of this paper, we use f_k to refer to the physical resolution of the model. Nonetheless, we stress that each f_k has a corresponding f_ε, f_a, and f_b given in Table II.

TABLE II. Modeled-to-total ratios, f_ϕ, used in the RT PANS computations at $0.00 < f_k < 1.00$.

	f_k	0.25	0.35	0.50
S_1	f_ε	1.00	1.00	1.00
	f_a	1.00	1.00	1.00
	f_b	1.00	1.00	1.00
S_2	f_ε	1.00	1.00	1.00
	f_a	0.50	0.59	0.71
	f_b	1.00	1.00	1.00
S_3	f_ε	1.00	1.00	1.00
	f_a	0.15	0.20	0.25
	f_b	0.25	0.35	0.50

IV. FLOWS AND SIMULATION DETAILS

A. Taylor-Green vortex

The Taylor-Green vortex flow [36] is a canonical test case used to investigate the modeling and simulation of onset, development, and decay of turbulence [40,86–100]. The flow is initially characterized by multiple laminar, well-characterized, and single-mode vortices. These are illustrated in Fig. 10, and defined by [36,87]

$$V_1(\mathbf{x}, t_o) = V_o \sin(x_1)\cos(x_2)\cos(x_3), \tag{78}$$

$$V_2(\mathbf{x}, t_o) = -V_o \cos(x_1)\sin(x_2)\cos(x_3), \tag{79}$$

$$V_3(\mathbf{x}, t_o) = 0, \tag{80}$$

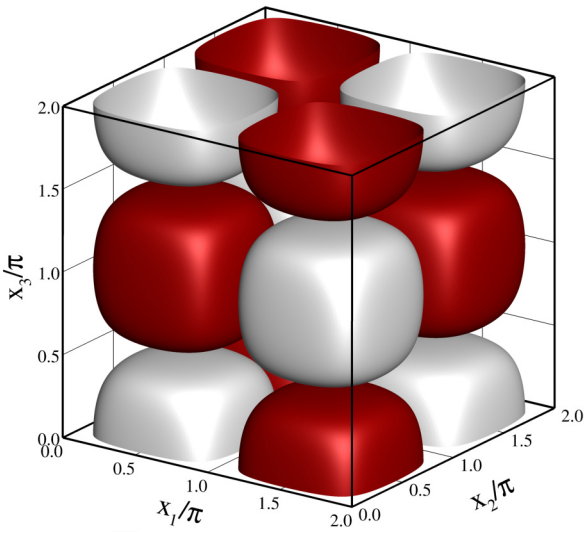

FIG. 10. Vortical structures present in the Taylor-Green vortex flow at $t = 0$. Structures defined by the isosurfaces of the vorticity x_3 component.

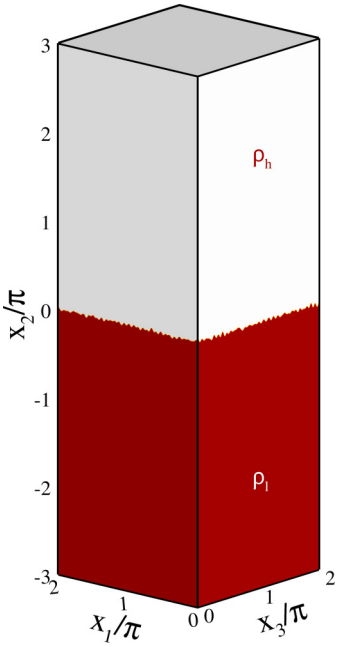

FIG. 11. Density field of the Rayleigh-Taylor flow at $t = 0$.

where V_o is the initial velocity magnitude. The corresponding pressure field is obtained from solving the Poisson equation,

$$P(\mathbf{x}, t_o) = P_o + \frac{\rho_o V_o^2}{16}[2 + \cos(2x_3)][\cos(2x_1) + \cos(2x_2)], \tag{81}$$

where P_o and ρ_o are the pressure and density at $t = 0$. The vortical structures of Fig. 10 interact and evolve in time, and vortex stretching processes generate vortex-sheets that gradually get closer. Afterward, these vortex-sheets roll up and reconnect [86,101], leading to the onset of turbulence and subsequent intensification of vorticity. The coherent structures break down and high-intensity turbulence appears. Finally, the turbulence kinetic energy dissipates rapidly by the action of viscous effects.

The analyzed TGV flow is characterized by a Reynolds number $\mathrm{Re} \equiv \rho L_o V_o/\mu = 3000$ [87,89] and an initial Mach number $\mathrm{Ma}_o = 0.28$. Such a Ma_o leads to maximum instantaneous and averaged (L_1 norm) variations of ρ smaller than 11.0% and 1.4% of ρ_o for $f_k = 0.00$, respectively. The computational domain of this problem is a cube with length equal to $L = 2\pi L_o$. Periodic boundary conditions are applied on all boundaries. The initial thermodynamic and flow properties are the following: $V_o = 10^4$ cm/s, $L_o = 1.00$ cm, $\rho_o = 1.178 \times 10^{-3}$ g/cm^3, $P_o = 10^5$ Pa, $\mu = 3.927 \times 10^{-3}$ g/(cm s), heat capacity ratio $\gamma = 1.40$, $k_o = 10^{-7}$ cm^2/s^2, and $S_o = 6.136 \times 10^{-3}$ cm.

B. Rayleigh-Taylor flow

The RT flow [3,4] is a benchmark problem of variable-density turbulent mixing, which has been intensely studied through numerous numerical experiments [102–111]. Its importance to the variable-density flow community motivated diverse validation initiatives such as the Alpha-Group collaboration [103].

The flow is initially characterized by a perturbed interface separating two fluids of different densities, Fig. 11. These materials are at rest, and the dense fluid, ρ_h, is on top of the light medium, ρ_l. The Atwood number of the flow is defined as $\mathrm{At} \equiv (\rho_h - \rho_l)/(\rho_h + \rho_l)$. After this instant, the

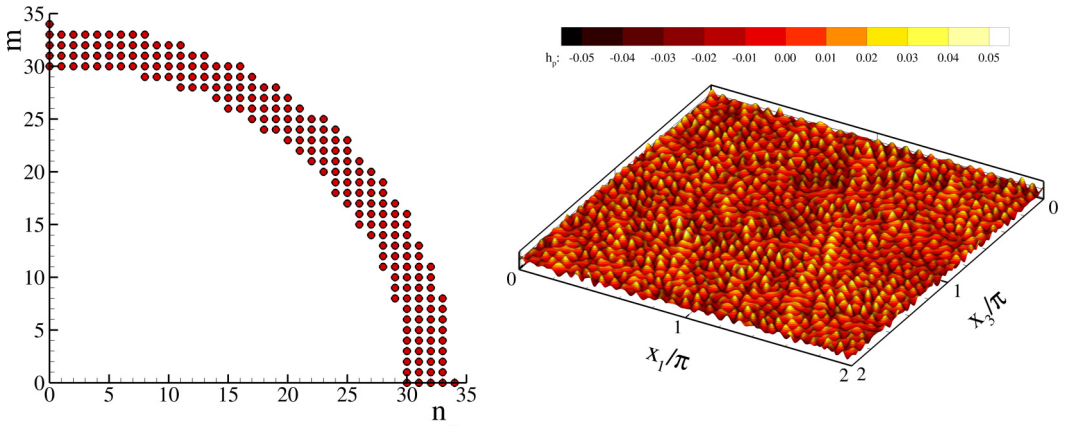

(a) Wave-number space (b) Physical space

FIG. 12. Initial perturbations at the interface ($x_2 = 0$) in wave-number (modes) and physical space.

heavy fluid starts accelerating downward by the action of gravity, whereas the light material moves upward. The interface perturbations create a misalignment between the density gradient and the pressure, which induces the RT instability. The resulting upward-moving structures, named bubbles, are the penetration of heavy fluid into the light medium, and, conversely, downward-moving spikes are the penetration of light fluid into the heavy medium. The shearing motion on the edges of these coherent structures triggers a Kelvin-Helmholtz instability, leading to the onset and development of turbulence. As a result, the mixing rate of the two materials and the mixing-layer width increase. The temporal evolution of the RT flow comprises a linear (laminar flow) and a nonlinear (laminar, transitional, and turbulent flow) regime. A comprehensive description of the flow is given by Sharp [112], Zhou [81,82], and Boffeta and Mazzino [113].

The flow configuration analyzed here is based on the DNS of Livescu *et al.* [114] at At $= 0.5$. The computational domain is a rectangular prism defined in a Cartesian coordinate system (x_1, x_2, x_3), Fig. 11. Its cross-section is $L = 2\pi$ cm wide, and the height is $3L$ to ensure a negligible influence of the vertical boundaries on the simulations during the simulated time $T = 25$ time-units [time normalized by $t^* = \sqrt{(L/(32g\text{At}))}$ [114]]. The bulk Reynolds number defined as $\text{Re} \equiv h\dot{h}/\nu$ can reach $\text{Re} \approx 500$ for the current settings (h and $\dot{h}$ are the mixing-layer height and its temporal derivative). Periodic boundary conditions are applied on the lateral walls and reflective conditions on the vertical boundaries, $x_2 = \pm 1.5L$. The domain height and simulation time guarantee that the simulations are not disturbed by the latter boundary condition.

The location of the interface between the two fluids is perturbed by

$$h_p(x_1, x_3) = \sum_{n,m} \cos\left[2\pi\left(n\frac{x_1}{L} + r_1\right)\right] \cos\left[2\pi\left(m\frac{x_3}{L} + r_3\right)\right]. \tag{82}$$

These perturbations possess wavelengths ranging from modes 30 to 34 ($30 \leqslant \sqrt{n^2 + m^2} \leqslant 34$), and amplitudes with standard-deviation not exceeding $0.04L$ [99,106], Fig. 12. Note that m and n are selected to include the most unstable mode of the linearized problem [114,115]. In Eq. (82), r_1 and r_3 are random numbers between 0 and 1. The numerical experiments rely on the ideal-gas equation of state, and the initial temperature is set to maintain the flow $\text{Ma} < 0.10$ and guarantee incompressible flow. The initial thermodynamic and flow properties are defined as follows: $\mu_l = 0.002$ g/(cm s), $\mu_h = 0.006$ g/(cm s), $\rho_l = 1.0$ g/cm^3, $\rho_h = 3.0$ g/cm^3, $\gamma_l = \gamma_h = 1.40$, $g = -980$ cm/s^2, $k_o = 10^{-6}$ cm^2/s^2, $S_o = 10^{-6}$ cm, and Schmidt and Prandtl numbers are set equal to 1.

C. Numerical settings

All calculations are conducted with the flow solver xRAGE [116]. This code utilizes a finite volume approach to solve the compressible and multimaterial conservation equations for mass, momentum, energy, and species concentration. The resulting system of governing equations is resolved [117] through the Harten–Lax–van Leer–Contact [118] Riemann solver using a directionally unsplit strategy, direct remap, parabolic reconstruction [119], and the low Mach number correction proposed by Thornber *et al.* [120]. The equations are discretized with second-order accurate methods: the spatial discretization is based on a Godunov scheme, whereas the temporal discretization relies on an explicit Runge-Kutta scheme known as Heun's method. The time-step, Δt, is defined by prescribing the maximum instantaneous CFL number,

$$\Delta t = \frac{\Delta x \times \mathrm{CFL}}{3(|V| + c)}, \tag{83}$$

where c is the speed of sound, and Δx is the grid cell size. The CFL is set equal to 0.45 for the TGV and 0.50 for the RT. The code can utilize an Adaptive Mesh Refinement (AMR) algorithm for following waves, especially shock-waves and contact discontinuities. This option is not used in the work to prevent hanging-nodes [121], and the simulations use orthogonal uniform hexahedral grids. For the TGV, these have 512^3 elements for simulations at $f_k \geqslant 0.25$, and 1024^3 cells for computations at $f_k = 0.00$. This option keeps the numerical accuracy of computations at different f_k uniform [40]. On the other hand, the RT uses a mesh with $256^2 \times 768$ cells [41].

xRAGE models miscible material interfaces and high convection-driven flows with a van-Leer limiter [123], without artificial viscosity, and no material interface treatments [124,125]. The solver uses the assumption that cells containing more than one material are in pressure and temperature equilibrium as a mixed cell closure. The effective kinematic viscosity in multimaterial problems [100] is defined as

$$\nu = \sum_{n=1}^{n_t} \nu_n f_n, \tag{84}$$

where n is the material index, n_t is the number of materials, and f_n is the volume fraction of material n. For the RT flow, the diffusivity $\mathcal{D}$ and thermal conductivity κ are defined by imposing Schmidt ($\mathrm{Sc} \equiv \nu/\mathcal{D}$) and Prandtl ($\mathrm{Pr} \equiv c_p\mu/\kappa$) numbers equal to 1.

The RT computations test all three strategies for setting the parameters f_ϕ given is Sec. III A 3. For the TGV simulations, where there are no a_{i_u} and b_u equations, the three strategies are equivalent.

V. RESULTS AND DISCUSSION

This section summarizes the TGV and RT results to illustrate the accuracy and potential of the proposed variable-density PANS formulation. Additional details of the TGV results are given in Pereira *et al.* [40]. More detailed analysis of the RT will be the subject of a subsequent manuscript [41]. Apart from two- and three-dimensional field plots, all results have been spatially averaged.

A. Taylor-Green vortex

As previously mentioned, the TGV initially features the laminar, single-mode, and well-defined vortical structures depicted in Fig. 10. Immediately after $t = 0$, these coherent structures start interacting and deforming, leading to vortex-stretching processes that generate the pairs of long sheetlike vortices observed in Fig. 13 at $t = 3.0$. Between $t = 3.0$ and 7.0, these structures get closer and undergo a complex vortex-reconnection mechanism [40,87,101] between pairs of counter-rotating vortices, Fig. 13(b). This triggers the onset of the turbulence at $t \approx 7.0$. Figure 13(c) shows the bursts of small turbulence scales at this instant. Afterward, turbulence further develops and eventually decays. This is illustrated in Figs. 13(d)–13(f). Considering the flow evolution, the physics of the

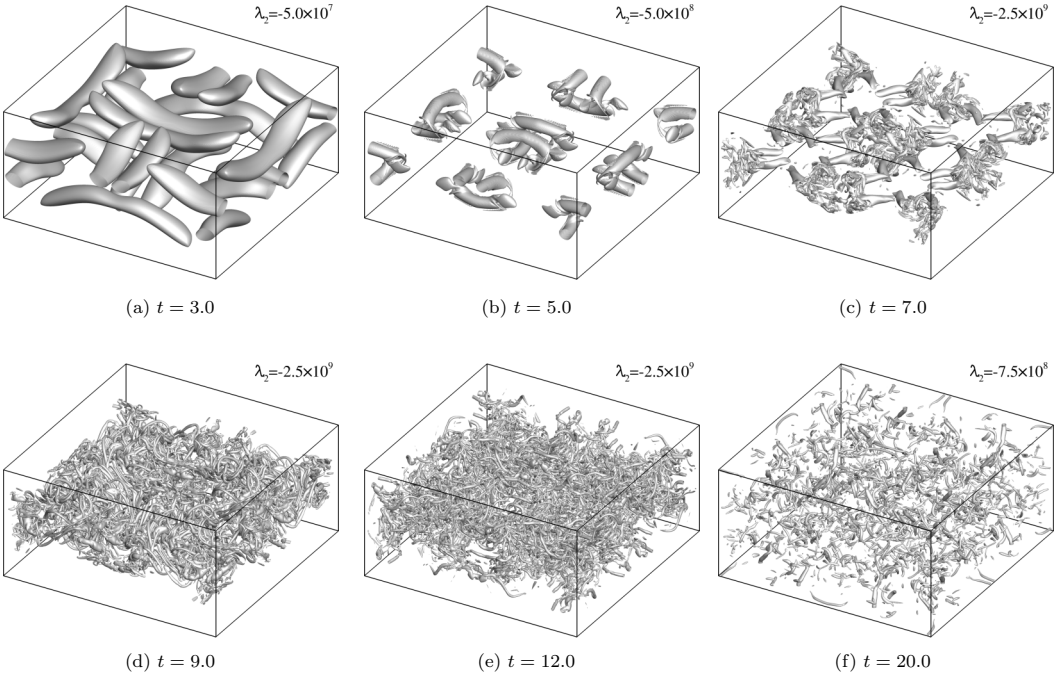

FIG. 13. Temporal evolution of the coherent and turbulent structures of the TGV predicted with $f_k = 0.00$ [40]. Vortical structures identified with the λ_2 criterion [122].

first nine time-units is expected to pose the greatest challenges to modeling and simulation of the TGV flow.

Figure 14 presents the temporal evolution of the total kinetic energy, k, predicted by PANS BHR-LEVM at different degrees of physical resolution, f_k. Note that k comprises a resolved, k_r, and

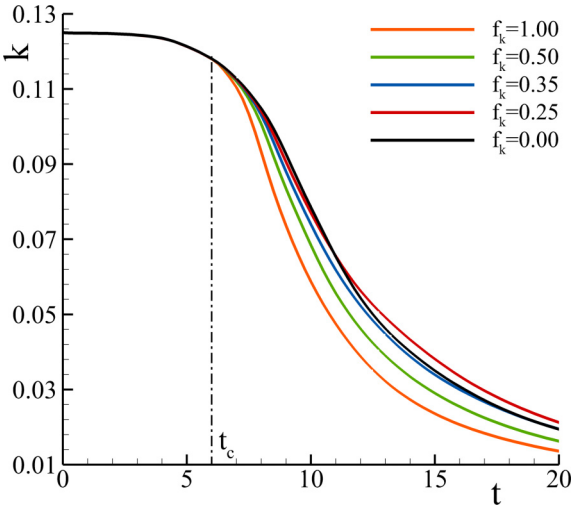

FIG. 14. Temporal evolution of the total kinetic energy, k, for predictions at different f_k.

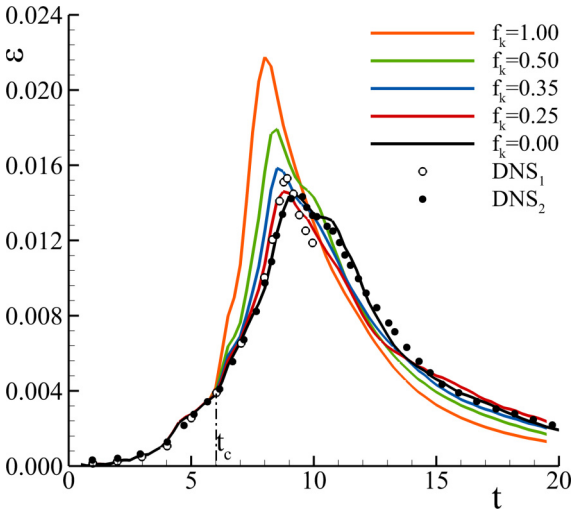

FIG. 15. Temporal evolution of the total kinetic energy dissipation, ε (s^{-1}), for predictions at different f_k.

unresolved, k_u, component,

$$k = k_r + k_u, \tag{85}$$

which are obtained from the resolved velocity field and the turbulence closure, respectively. It is important to stress that the resolved component of k comprises a nonturbulent [46] and turbulent component, while the unresolved part entails the turbulent fraction of k being modeled. The results indicate that k is initially nearly constant, and independent of f_k until $t = t_c \approx 6.0$. At this instant, in which the flow undergoes vortex-reconnection processes, the simulations become strongly dependent on f_k. This result allows us to categorize the simulations into high- (HPR, $f_k < 0.50$) and low- (LPR, $f_k \geqslant 0.50$) physical resolution. The data show that LPR simulations lead to a pronounced nonphysical decay of k. As discussed later, this is caused by a rapid increase and overprediction of the modeled turbulent stresses. In contrast, HPR computations exhibit smaller energy decay rates and, as such, larger values of k at late times. Yet, the most significant result of Fig. 14 is that the solutions converge upon physical resolution refinement ($f_k \to 0$). It also shows that all HPR solutions are in good agreement. This behavior is particularly evident until $t = 10$.

Next, Fig. 15 depicts the temporal evolution of the dissipation of total kinetic energy, ε,

$$\varepsilon = -\frac{dk}{dt}, \tag{86}$$

and compares the results against the DNS of Brachet *et al.* [87] at Ma = 0 (DNS_1) and Drikakis *et al.* [89] at Ma = 0.28 (DNS_2). The results exhibit similar tendencies to those of k. Until $t = t_c$, all simulations are independent of the physical resolution and in excellent agreement with the reference DNS solutions. After this instant, the computations become closely dependent on f_k, but their solutions converge toward the reference DNS data upon physical resolution refinement, $f_k \to 0$. Most notably, it is once again possible to distinguish between HPR and LPR computations. The first show a diminishing dependence on f_k, and a good agreement with the reference numerical experiments [87,89]. Considering the cases at $f_k \leqslant 0.25$, the maximum values of ε at $8.8 \leqslant t \leqslant 9.3$ range from 0.145 to 0.146, whereas the DNS studies report values between 0.143 and 0.153. The largest discrepancies between HPR and DNS computations occur at late times. These are likely caused by numerical uncertainty and compressibility effects [40,126].

On the other hand, LPR computations lead to large discrepancies compared to the reference DNS studies. The peak of dissipation occurs prematurely, and its magnitude is clearly overpredicted.

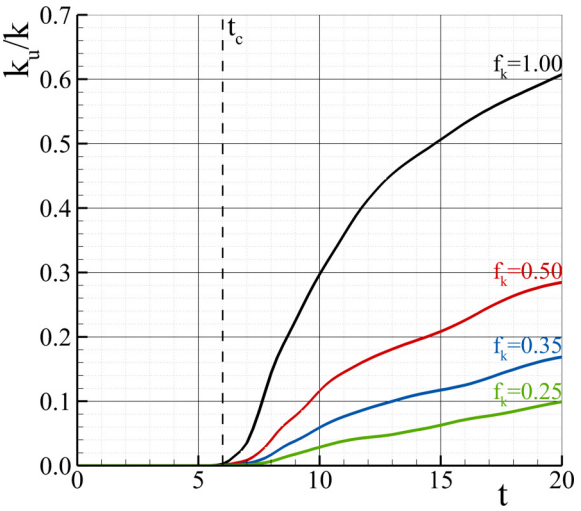

FIG. 16. Temporal evolution of the ratio modeled-to-total kinetic energy, k_u/k, for predictions at different f_k.

As for k, the differences grow as the physical resolution coarsens, $f_k \to 1.0$. For instance, the magnitude of the dissipation peak can reach 0.218 ($f_k = 1.00$), exceeding the value reported by the reference DNS studies by more than 50%. Also, the dissipation peak occurs at $t \approx 8$ instead of between $t = 9$ and 9.3 [87,89].

The results of Figs. 14 and 15 suggest that LPR simulations prematurely predict the onset of turbulence, overpredicting the unresolved turbulent stress tensor. This would explain the rapid decay of k observed in Fig. 14. These ideas are supported by the ratio of unresolved-to-total kinetic energy, k_u/k, depicted in Fig. 16. The data indicate that k_u/k is negligible and independent of f_k until $t = t_c$. After this instant, k_u/k grows considerably, and its magnitude becomes closely dependent on f_k. Also, it is visible that the growth of k_u/k starts earlier and it is more rapid for simulations at $f_k = 1.00$ than at $f_k = 0.25$. For example, k_u/k predicted at $t = 20$ and $f_k = 1.00$ is six times larger than that at $f_k = 0.25$. Considering the results for ε, this shows that simulations at $f_k = 1.00$ overpredict the turbulent stresses. We emphasize that transient flows are highly sensitive to history effects, and high-resolution PANS simulations showing $f_k \approx (f_k)_e = k_u/k_{u(f_k=1.00)}$ would indicate that the RANS closure can accurately represent the mean-flow field of the selected problem. This is often observed in statistically steady flows.

It is also interesting to note that k_u/k only starts growing rapidly at $t \geqslant 7.0$ for HPR simulations. As shown in Fig. 13, this corresponds to the instant when the onset of turbulence is expected to occur [87]. Hence, we can infer that LPR simulations misrepresent the onset of turbulence due to the overprediction of the unresolved turbulent stress tensor, leading to a poor prediction of the vortex-reconnection process and consequent premature onset of turbulence. This is illustrated in Fig. 17, which depicts the coherent and turbulent flow structures predicted at $t = 6.5$ at representative values of f_k. The plots show that the LPR simulation ($f_k = 1.00$) dissipates the laminar coherent structures involved in the vortex-reconnection processes. This is caused by the overprediction of turbulence since ν_t [see Eq. (17)] can exceed its laminar counterpart by a factor of 30. This does not occur at $f_k = 0.35$ (highest HPR f_k) nor at $f_k = 0.00$. A comprehensive assessment of this flow is given in [40].

In summary, the results indicate that the proposed PANS BHR-LEVM model can accurately predict the shear driven TGV flow using $f_k < 0.50$. At such values of f_k, the computations exhibit a relatively small dependence on the physical resolution and are able to resolve the phenomena not amenable to straightforward closure modeling. Next, we evaluate the performance of the model predicting the buoyancy-driven RT flow.

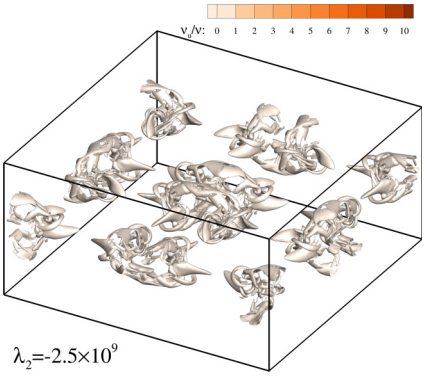

(a) $f_k = 0.00$

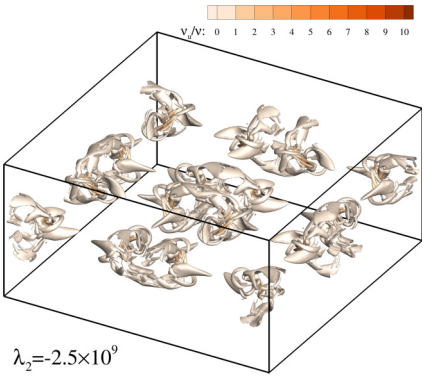

(b) $f_k = 0.35$

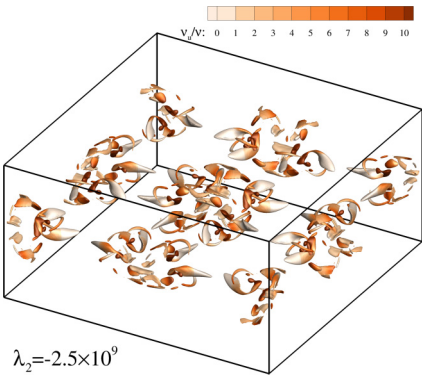

(c) $f_k = 1.00$

FIG. 17. Temporal evolution of the coherent and turbulent structures of the TGV at $t = 6.5$ predicted with different f_k [40]. Vortical structures identified with the λ_2 criterion [122].

B. Rayleigh-Taylor

The present RT flow is initialized with the perturbed interface shown in Figs. 12 and 18(a). Immediately after this instant, the two fluids accelerate, and the interface perturbations create a misalignment between the density gradient and the pressure. This leads to the generation of coherent structures called spikes and bubbles [81,82] with the mushroomlike shape illustrated in Figs. 18(c)–18(e) and 19(a) at $t \leqslant 2.5$. During this period, the flow is laminar, and it is in the

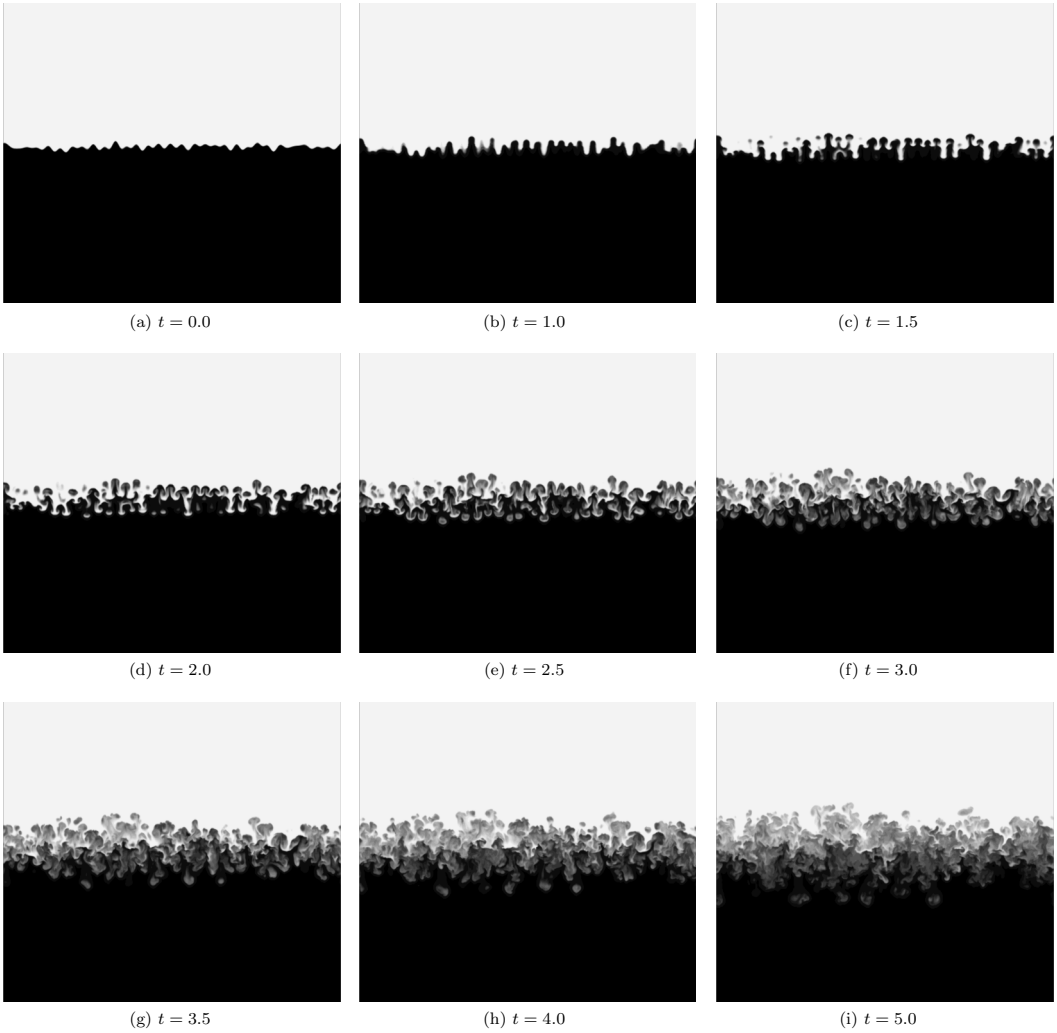

(a) $t = 0.0$ (b) $t = 1.0$ (c) $t = 1.5$

(d) $t = 2.0$ (e) $t = 2.5$ (f) $t = 3.0$

(g) $t = 3.5$ (h) $t = 4.0$ (i) $t = 5.0$

FIG. 18. Temporal evolution of the RT density field predicted at early flow stages using $f_k = 0.00$ (2D plane).

so-called linear regime [81,82]. In the following instants, Figs. 18(f)–18(i) and 19(b)–19(d), the mixing-layer continues growing, and the initially linear structure and the Kelvin-Helmholtz secondary instability will eventually trigger the onset and development of turbulence. This phenomenon increases the mixing rate and enhances the mixture homogeneity, occurring in the nonlinear regime [81,82]. It is particularly pronounced at $t = 20.0$ [Fig. 19(d)]. As in the TGV case, the onset and development of turbulence is expected to pose major challenges to modeling and simulation of the RT problem.

To evaluate the accuracy of the PANS BHR-LEVM model, Figs. 20 and 21 depict the evolution of the mixing-layer height, h, and density field, χ, predicted at different f_k. Also, the simulations test the three strategies proposed in Sec. III A 3 to define the relationship between the parameters f_ϕ (f_k, f_ε, f_a, and f_b). Here, the quantity $\overline{\chi}$ used to analyze the density field is defined as

$$\overline{\chi} = \frac{\overline{\rho} - \rho_l}{\rho_h - \rho_l}. \tag{87}$$

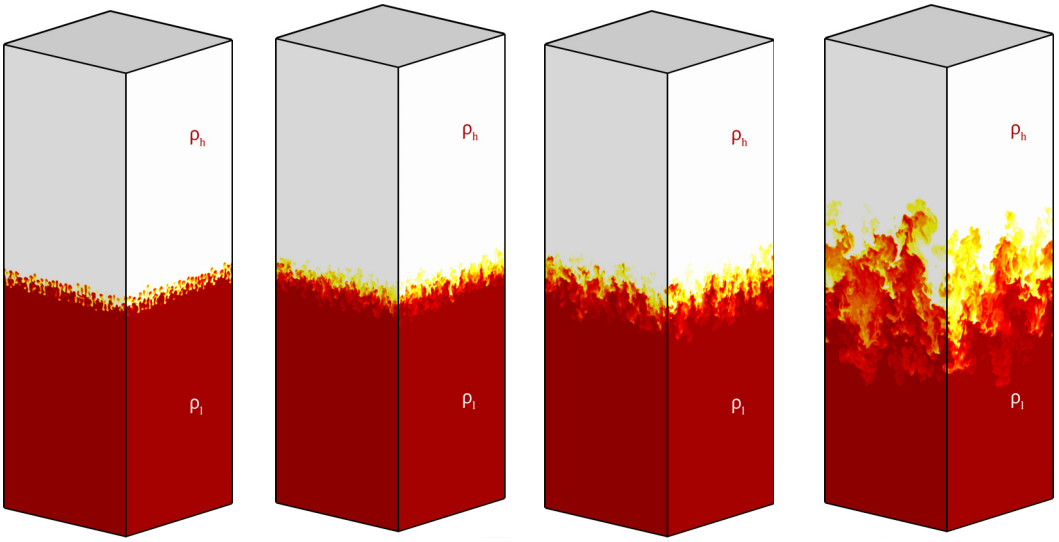

(a) $t = 2.5$ (b) $t = 5.0$ (c) $t = 10.0$ (d) $t = 20.0$

FIG. 19. Temporal evolution of the RT density field predicted with $f_k = 0.00$.

The mixing-layer width h is defined as the distance between the locations $\bar{\chi} = 0.05$ and 0.95, where here the bar indicates a planar average normal to gravity. Both h and x_2 are normalized by L. Since the physics and statistics of RT flow are highly dependent on initial conditions and settings, we use the solutions obtained at $f_k = 0.00$ as a reference.

Figure 20 indicates that the simulations are closely dependent on the value of f_k, and they converge upon this parameter's refinement (except S_3), $f_k \to 0.00$. Comparing the solution at $f_k = 0.00$ against that at $f_k = 1.00$ shows that the second case leads to a significantly thicker mixing-layer at late times, and a shorter linear region ($t < 2$). Once again, this result suggests that the simulation at $f_k = 1.00$ prematurely predicts the onset of turbulence by overpredicting the total turbulent stresses. The refinement of f_k improves the simulations by reducing the discrepancies against the reference solution ($f_k = 0.00$). Also, Fig. 20 illustrates that all solutions at $f_k \leqslant 0.25$ are in good agreement.

The exceptions are the simulations using S_3. The data indicate that this approach leads to poorer results than the remaining strategies, which do not improve for $f_k \leqslant 0.35$ (recall that $f_k = 0.00$ does not use a turbulence closure). This outcome stems from the fully developed turbulence assumption embedded in this strategy, which is not verified at early flow stages. As comprehensively discussed in [41], S_3 leads to an inconsistent definition of f_ϕ at early flow stages and, consequently, to large modeling errors and numerical robustness issues. The latter increase upon grid resolution refinement. This result illustrates the importance of a precise and robust selection of f_ϕ. Regarding the remaining strategies, S_2 leads to the smallest comparison errors between simulations ($f_k > 0$) and the reference solution.

Figure 21 shows how the density field evolves in time and space with f_k. For conciseness, we only show three representative cases: $f_k = 0.00$, 0.25 (S_2), and 1.00. The remaining cases are in line with the results of Fig. 20. As for the quantity h, the results show distributions of $\overline{\chi}$ quite similar between solutions obtained at $f_k \leqslant 0.25$. In contrast, those obtained from simulations at $f_k = 1.00$ exhibit linear and smoother profiles. This behavior stems from the shortcomings of one-point closures to fully model ($f_k = 1.00$) transient turbulence and the fact that this modeling strategy does not resolve turbulence (lower numerical requirements).

Next, Fig. 22 presents the evolution of the maximum planar $(x_1 - x_3)$ averaged value of ν_u obtained at different physical resolutions. Note that ν_u is utilized here to evaluate how the unresolved

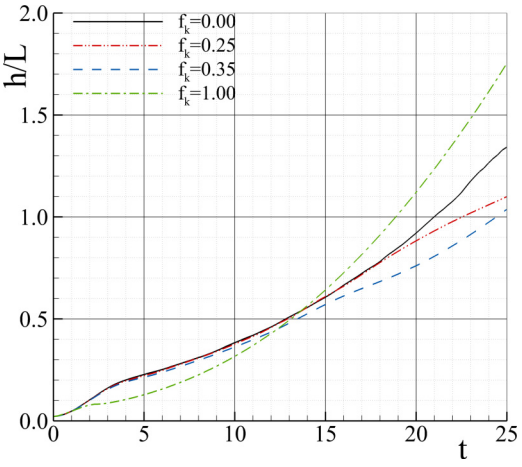

(a) S_1.

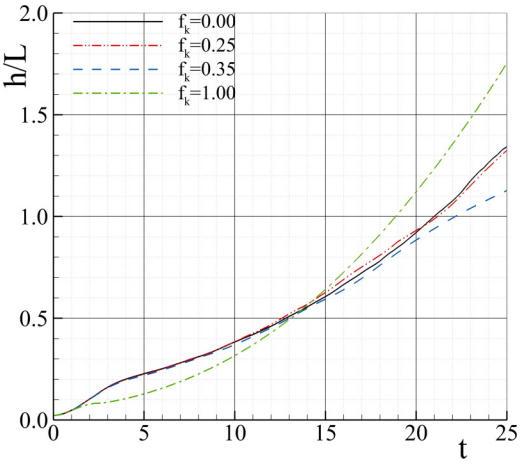

(b) S_2.

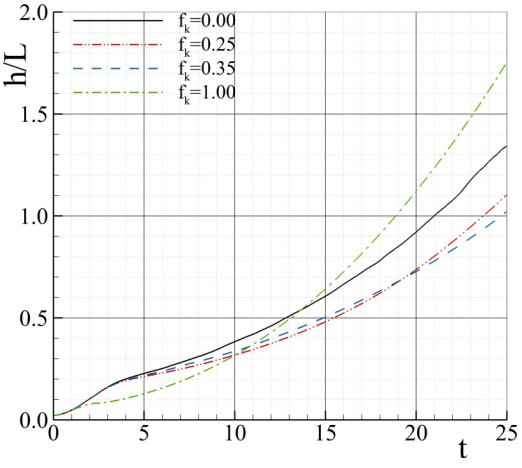

(c) S_3.

FIG. 20. Temporal evolution of the mixing-layer height, h, predicted with different f_k and S_i.

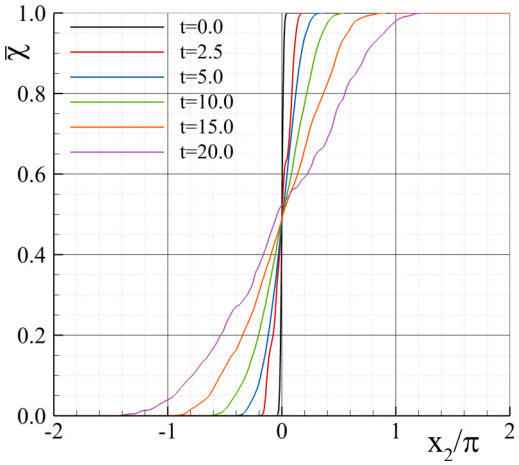

(a) $f_k = 0.00$.

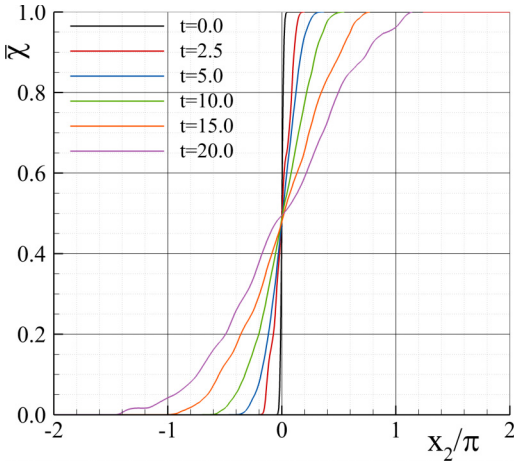

(b) $f_k = 0.25$ using S_1.

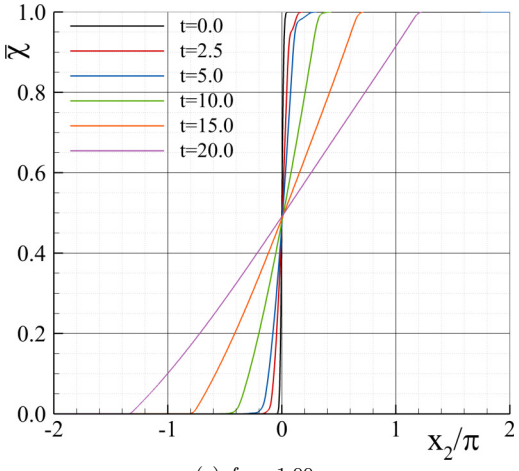

(c) $f_k = 1.00$.

FIG. 21. Temporal evolution of the density field, $\overline{\chi}$, predicted with different f_k.

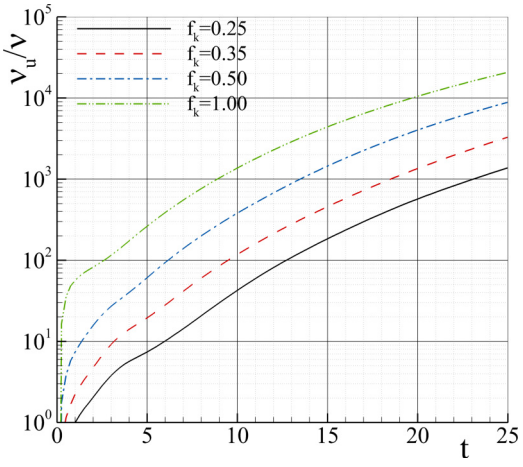

(a) S_1.

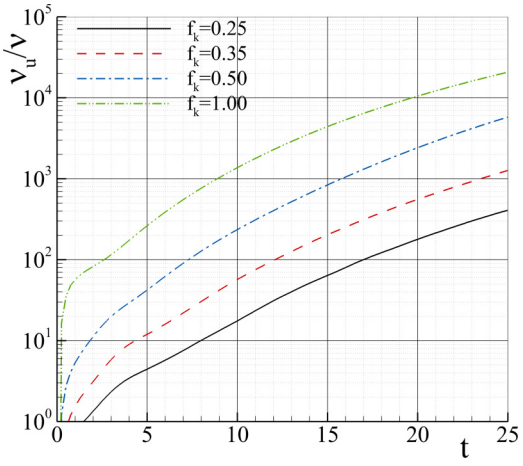

(b) S_2.

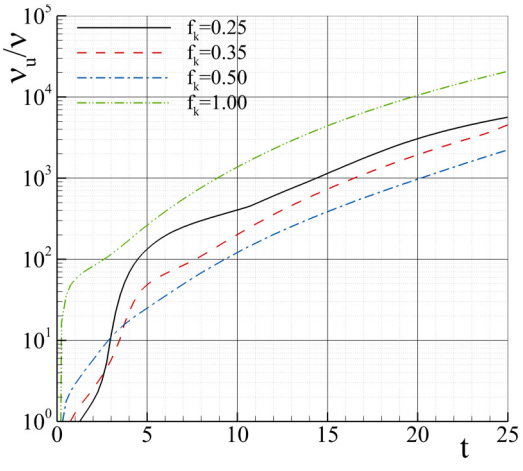

(c) S_3.

FIG. 22. Temporal evolution of the ratio ν_u/ν predicted with different f_k and S_i.

(a) $f_k = 0.25$ and S_1. (b) $f_k = 0.25$ and S_2. (c) $f_k = 1.00$.

FIG. 23. RT structures at $t = 2.5$ predicted with $f_k = 0.25$ (S_1 and S_2) and 1.00. Vortical structures identified through the density field (2D plane).

turbulent stresses evolve with f_k [see Eq. (17)]. Also, it is important to emphasize that ratios ν_u/ν exceeding $O(1)$ are usually attributed to turbulence effects. As expected, the results show that ν_u/ν decreases with f_k. Considering $t = 25$, ν_u/ν reduces from 20 736.6 at $f_k = 1.00$ to 1376.0 (S_1), 407.8 (S_2), and 5634.4 (S_3) at $f_k = 0.25$. The large values obtained with S_3 at the smallest f_k are caused by the aforementioned consistency issues selecting f_ϕ with this strategy. These results also show that the strategy used to define the relationship between the different f_ϕ has an important impact on the magnitude of ν_u and, consequently, $\tau^1(V_i, V_j)$.

However, the most significant result in Fig. 22 is the fact that ν_u/ν does not exceed 5.7 for $f_k = 0.25$ (S_1 and S_2) and $t \leqslant 4$ (linear regime and laminar flow), whereas this quantity exceeds 173.7 for $f_k = 1.00$. Such a result indicates that the simulation with $f_k = 1.00$ leads to a premature onset of turbulence. On the other hand, PANS at $f_k = 0.25$ can capture the coherent structures that are subsequently involved in the onset and development of turbulence. This outcome explains the results of Figs. 20 and 21 and can be seen in Fig. 23, in which the flow coherent structures are depicted for $f_k = 0.25$ (S_1 and S_2) and 1.00 at $t = 2.5$. Compared to Fig. 18, the results show that simulations at $f_k = 1.00$ dissipate the laminar coherent structures. This is caused by the overprediction of turbulence, i.e., the magnitude of ν_t or $\tau^1(V_i, V_j)$. In clear contrast, simulations at $f_k = 0.25$ can accurately predict these coherent structures, this being the reason for the good agreement between simulations at $f_k \leqslant 0.25$ (S_1 and S_2). Hence, the RT computations reinforce the importance of resolving the flow phenomena not amenable to modeling to obtain efficient high-fidelity simulations [22].

Overall, the results have shown that the PANS BHR-LEVM model can predict the current RT flow accurately using sufficiently small values of f_k. Regarding the strategies to prescribe f_ϕ, S_2 leads to the lowest values of ν_u, allowing the utilization of larger f_k than S_1. S_3 causes consistency issues between the different f_ϕ due to the fully developed turbulence assumption. A comprehensive analysis of this problem is given in a subsequent paper.

VI. CONCLUSIONS

We extended the framework of the PANS model to variable-density flow, i.e., multi-material and/or compressible mixing problems including density fluctuations and production of turbulence kinetic energy by shear and buoyancy mechanisms. The framework was utilized to derive the PANS version of the k-S-a_i-b equation BHR-LEVM closure. The parameters defining the physical resolution of the model (f_k, f_ε, f_a, and f_b) have been studied through *a priori* testing. Three strategies are proposed to set these parameters as a function of f_k: (i) define $f_\varepsilon = f_{a_i} = f_b = 1.0$; (ii) prescribe $f_{a_i} = \sqrt{f_k}$ and $f_\varepsilon = f_b = 1.0$; and (iii) set $f_\varepsilon = 1.0$, $f_a = 0.5 f_k$, and $f_b = f_k$. The first two strategies lead to high-fidelity simulations, whereas the third leads to consistency issues between different f_ϕ. Thus, S_1 and, in particular, S_2 seem better approaches to select f_ϕ. Future studies will further

investigate these strategies. The initial validation space of the PANS BHR-LEVM model comprises the TGV at $\mathrm{Re} = 3000$ and the RT at $\mathrm{At} = 0.5$ and $(\mathrm{Re})_{\max} \approx 500$ flows. The results are promising and confirm the ability of the model to calculate these representative flows accurately. Hence, this initial validation space and the theoretical justification demonstrate the new methodology's potential to predict complex problems of variable-density flow. Nevertheless, subsequent studies will be needed to study and extend the validation space of the model further. Finally, all simulations indicate the importance of resolving the phenomena not amenable to modeling by the closure. This dictates the required physical resolution to obtain high-fidelity simulations.

ACKNOWLEDGMENTS

We would like to thank C. B. da Silva, D. Aslangil, and D. Livescu for sharing their DNS data sets. Also, we would like to thank the two reviewers for their suggestions that improved our paper. Los Alamos National Laboratory (LANL) is operated by TRIAD National Security, LLC for the U.S. DOE NNSA. This research was funded by LANL Mix and Burn project under the DOE ASC, Physics and Engineering Models program.

[1] H. von Helmholtz, On discontinuous movements of fluids, London, Edinburgh, Dublin Philos. Mag. J. Sci. **36**, 337 (1868).
[2] W. Thomson, Hydrokinetic solutions and observation, London, Edinburgh, Dublin Philos. Mag. J. Sci. **42**, 362 (1871).
[3] L. Rayleight, Investigation of the character of the equilibrium of an incompressible heavy fluid of variable density, Proc. London Math. Soc. **14**, 170 (1882).
[4] G. Taylor, The instability of liquid surfaces when accelerated in a direction perpendicular to their planes, Proc. R. Soc. Lond. A **201**, 192 (1950).
[5] R. Richtmyer, Taylor instability in shock acceleration of compressible fluids, Commun. Pure Appl. Math. **13**, 297 (1960).
[6] E. Meshkov, Instability of the interface of two gases accelerated by a shock wave, Sov. Fluid Dyn. **4**, 101 (1969).
[7] J. Smagorinsky, General circulation experiments with the primitive equations I. The basic experiment, Mon. Weather Rev. **91**, 99 (1963).
[8] O. Reynolds, On the dynamical theory of incompressible viscous fluids and the determination of the criterion, Philos. Trans. R. Soc. London **186**, 123 (1985).
[9] A. Favre, Équations statistiques des gaz turbulens, C. R. Acad. Sci. Paris **246** (1958).
[10] A. Favre, Équations statistiques des gaz turbulens compressibles. I. Formes générales, J. Mec. **4**, 361 (1965).
[11] A. Favre, Équations statistiques des gaz turbulens compressibles. II. Méthode des vitesses moyennes; Méthod des vitesses macroscopiques pondérées par la masse volumique, J. Mec. **4**, 391 (1965).
[12] A. Favre, Équations statistiques aux fluctuations d'entropie, de concentration, de rotationnel dans les écoulements compressibles, C. R. Acad. Sci. Paris **273**, 1289 (1971).
[13] D. Besnard, F. H. Harlow, R. M. Rauenzahn, and C. Zemach, Turbulence transport equations for variable-density turbulence and their relationship to two-field models, Tech. Rep. LA-12303-MS, DE92 017292 (Los Alamos National Laboratory, 1992).
[14] P. Chassaing, The modeling of variable density turbulent flow, Flow, Turbul. Combust. **66**, 293 (2001).
[15] P. Chassaing, R. Antonia, F. Anselmet, L. Joly, and S. Sarkar, in *Variable Density Fluid Turbulence*, edited by R. Moreau, Fluid Mechanics and Its Applications Vol. 69 (Springer-Science+Business Media, B.V., 2002).
[16] D. Wilcox, *Turbulence Modeling for CFD*, 3rd ed. (DCW Industries, La Cañada, USA, 2006).
[17] A. K. M. F. Hussain and W. C. Reynolds, The mechanics of an organized wave in turbulent shear flow, J. Fluid Mech. **41**, 241 (1970).

[18] R. Schiestel, Multiple-time-scale modeling of turbulent flows in one-point closures, Phys. Fluids **30**, 722 (1987).
[19] M. Germano, Turbulence: The filtering approach, J. Fluid Mech. **238**, 325 (1992).
[20] M. Germano, From RANS to DNS: Towards a Bridging Model, in *Direct and Large-Eddy Simulation III, ERCOFTAC Series* (Springer, The Netherlands, 1999), pp. 225–236.
[21] C. Speziale, Computing Non-Equilibrium Turbulent Flows With Time-Dependent RANS and VLES, in *15th International Conference on Numerical Methods in Fluid Dynamics*, Lecture Notes in Physics Vol. 490, edited by P. Kutler and J. F. J. Chattot (Springer, Berlin, 1997).
[22] F. S. Pereira, L. Eça, G. Vaz, and S. S. Girimaji, Challenges in scale-resolving simulations of turbulent wake flows with coherent structures, J. Comput. Phys. **263**, 98 (2018).
[23] P. Batten, U. Goldberg, and S. Chakravarthy, Sub-Grid Turbulence Modeling for Unsteady Flow With Acoustic Resonance, in *38thAmerican Institute of Aeronautics and Astronautics Aersopaces Science Meeting and Exhibit*, AIAA-00-0473 (Reno, NV, 2000).
[24] H. Fasel, J. Seidel, and S. Wernz, A methodology for simulations of complex turbulent flows, J. Fluids Eng. **124**, 993 (2002).
[25] R. Schiestel and A. Dejoan, Towards a new partially integrated transport model for coarse grid and unsteady turbulent flow simulations, Theor. Comput. Fluid Dyn. **18**, 443 (2005).
[26] B. Chaouat and R. Schiestel, A new partially integrated transport model for subgrid-scale stresses and dissipation rate for turbulent developing flows, Phys. Fluids **17**, 065106 (2005).
[27] S. S. Girimaji, Partially-averaged navier-stokes model for turbulence: A reynolds-averaged navier-stokes to direct numerical simulation bridging method, J. Appl. Mech. **73**, 413 (2005).
[28] F. S. Pereira, L. Eça, and G. Vaz, Investigating the effect of the closure in partially-averaged navier-stokes equations, J. Fluids Eng. **141**, 121402 (2019).
[29] K. Stalsberg-Zarling and R. Gore, *The BHR2 Turbulence Model: Incompressible Isotropic Decay, Rayleigh-Taylor*, Kelvin-Helmholtz and Homogenous Variable Density Turbulence, Tech. Rep. LA-UR-11-04773 (Los Alamos National Laboratory, 2011).
[30] J. D. Schwarzkopf, D. Livescu, J. R. Baltzer, R. A. Gore, and J. R. Ristorcelli, A two-length scale turbulence model for single-phase multi-fluid mixing, Flow, Turbul. Combust. **96**, 1 (2016).
[31] S. S. Girimaji, E. Jeong, and R. Srinivasan, Partially averaged Navier-Stokes method for turbulence: Fixed point analysis and comparison with unsteady partially averaged Navier-Stokes, J. Appl. Mech. **73**, 422 (2006).
[32] F. Hamba, Analysis of filtered Navier-Stokes equation for hybrid RANS/LES simulation, Phys. Fluids **23**, 015108 (2011).
[33] S. S. Girimaji and S. Wallin, Closure modeling in bridging regions of variable-resolution (VR) turbulence computations, J. Turbul. **14**, 72 (2013).
[34] S. Suman and S. S. Girimaji, On the invariance of compressible Navier-Stokes and energy equations subject to density weighted filtering, Flow, Turbul. Combust. **85**, 383 (2010).
[35] A. Banerjee, R. A. Gore, and M. J. Andrews, Development and validation of a turbulent-mix model for variable-density and compressible flows, Phys. Rev. E **82**, 046309 (2010).
[36] G. I. Taylor and A. E. Green, Mechanism of the production of small eddies from large ones, Proc. R. Soc. A **158**, 499 (1937).
[37] L. Rayleigh, Investigation of the character of the equilibrium of an incompressible heavy fluid of variable density, Proc. London Math. Soc. **14**, 170 (1882).
[38] T. Trucano, M. Pilch, and W. Oberkampf, *General Concepts for Experimental Validation of ASCI Code Applications*, Technical Report SAND2002-0341 (Sandia National Laboratories, Albuquerque, NM, 2002).
[39] W. L. Oberkampf and C. J. Roy, *Verification and Validation in Scientific Computing*, 1st ed. (Cambridge University Press, Cambridge, UK, 2010).
[40] F. S. Pereira, F. F. Grinstein, D. M. Israel, R. Rauenzahn, and S. S. Girimaji, Modeling and simulation of transitional Taylor-Green vortex flow with the partially-averaged Navier-Stokes equations, Phys. Rev. Fluids **6**, 054611 (2021).

[41] F. S. Pereira, F. F. Grinstein, D. M. Israel, R. Rauenzahn, and S. S. Girimaji, Modeling and simulation of transitional Rayleigh-Taylor flow with the partially-averaged Navier-Stokes equations (unpublished).
[42] F. A. Williams, *Combustion Theory: The Fundamental Theory of Chemically Reacting Flow Systems*, 1st ed. (Addison-Wesley, Reading, MA, 1965).
[43] A. W. Cook, Enthalpy diffusion in multicomponent flows, Phys. Fluids **21**, 055109 (2009).
[44] J. Boussinesq, Essai sur la théorie des eaux courantes, Mémoires Présentés par Divers Savants à L'Académie des Sciences **23**, 335 (1877).
[45] F. S. Pereira, L. Eça, G. Vaz, and S. S. Girimaji, Toward predictive RANS and SRS computations of turbulent external flows of practical interest, Arch. Comput. Mech. Eng. (2021), doi:10.1007/s11831-021-09563-0.
[46] E. Palkin, R. Mullyadzhanov, M. Hadžiabdić, and K. Hanjalić, Scrutinizing URANS models in shedding flows: The case of cylinder in cross flow in the subcritical regime, Flow, Turbul. Combust. **97**, 1017 (2016).
[47] J. D. Schwarzkopf, D. Livescu, R. A. Gore, and R. M. R. J. R. Ristorcelli, Application of a second-moment closure model to mixing processes involving multicomponent miscible fluids, J. Turbul. **12**, 1 (2011).
[48] P. Tazraei and S. S. Girimaji, Scale-resolving simulations of turbulence: Equilibrium boundary layer analysis leading to near-wall closure modeling, Phys. Rev. Fluids **4**, 104607 (2019).
[49] F. S. Pereira, L. Eça, G. Vaz, and S. S. Girimaji, On the simulation of the flow around a circular cylinder at Re=140,000, Int. J. Heat Fluid Flow **76**, 40 (2019).
[50] F. S. Pereira, G. Vaz, and L. Eça, Evaluation of RANS and SRS methods for simulation of the flow around a circular cylinder in the sub-critical regime, Ocean Eng. **186**, 106067 (2019).
[51] C. H. K. Williamson, Vortex dynamics in the cylinder wake, Annu. Rev. Fluid Mech. **28**, 477 (1996).
[52] M. M. Zdravkovich, *Flow Around Circular Cylinders. Volume 1: Fundamentals*, 1st ed. (Oxford Science Publications, Oxford, UK, 1997).
[53] P. J. Roache, *Verification and Validation in Computational Science and Engineering*, 1st ed. (Hermosa, Albuquerque, NM, 1998).
[54] F. S. Pereira, G. Vaz, L. Eça, and S. S. Girimaji, Simulation of the flow around a circular cylinder at Re= 3900 with partially-averaged Navier-Stokes equations, Int. J. Heat Fluid Flow **69**, 234 (2018).
[55] F. S. Pereira, Towards predictive scale-resolving simulations of turbulent external flows, Ph.D. thesis, Instituto Superior Técnico, Lisbon, Portugal, 2018.
[56] S. B. Pope, *Turbulent Flows*, 1st ed. (Cambridge University Press, Cambridge, UK, 2000).
[57] P. A. Davidson, *Turbulence: An Introduction for Scientists and Engineers* (Oxford University Press, Oxford, 2006).
[58] S. S. Girimaji and K. S. Abdol-Hamid, Partially-Averaged Navier Stokes Model for Turbulence: Implementation and Validation, in *Proceedings of the 43rd American Institute of Aeronautics and Astronautics (AIAA) Aerospace Sciences Meeting and Exhibit* (AIAA 2005-502, Reno, NV, 2005).
[59] S. Lakshmipathy and S. S. Girimaji, Partially averaged Navier-Stokes (PANS) method for turbulence simulations: Flow past a circular cylinder, J. Fluids Eng. **132**, 121202 (2010).
[60] A. Elmiligui, K. S. A.-H. S. J. Massey, and S. P. Pao, Numerical Study of Flow Past a Circular Cylinder Using RANS, Hybrid RANS/LES and PANS Formulations, in *22nd Applied Aerodynamics Conference and Exhibit*, AIAA 2004-4959 (Providence, RI, 2004).
[61] B. Basara and Z. P. S. Girimaji, A new approach for the calculation of the cut-off resolution parameter in bridging methods for turbulent flow simulation, Int. J. Heat Fluid Flow **74**, 76 (2018).
[62] L. Davidson and C. Friess, A new formulation of f_k for the PANS model, J. Turbul. **20**, 322 (2019).
[63] F. S. Pereira, L. Eça, G. Vaz, and L. Eça, Verification and validation: The path to predictive scale-resolving simulations of turbulence, arXiv:2103.09899.
[64] T. S. Silva, M. Zecchetto, and C. B. da Silva, The scaling of the turbulent/non-turbulent interface at high reynolds numbers, J. Fluid Mech. **843**, 156 (2018).
[65] G. Batchelor, V. Canuto, and J. Chasnov, Homogeneous buoyancy-generated turbulence, J. Fluid Mech. **235**, 349 (1992).

[66] D. L. Sandoval, T. T. Clark, and J. J. Riley, Buoyancy-Generated Variable-Density Turbulence, in *IUTAM Symposium on Variable Density Low-Speed Turbulent Flows*, Fluid Mechanics and Its Applications Vol. 41, edited by L. Fulachier, J. L. Lumley, and F. Anselmet (Springer, Dordrecht, The Netherlands, 1997), pp. 173–180.
[67] D. Livescu and J. R. Ristorcelli, Buoyancy-driven variable-density turbulence, J. Fluid Mech. **591**, 43 (2007).
[68] D. Livescu and J. R. Ristorcelli, Variable-density mixing in buoyancy-driven turbulence, J. Fluid Mech. **605**, 145 (2008).
[69] D. Aslangil, D. Livescu, and A. Banerjee, Variable-density buoyancy-driven turbulence with asymmetric initial density distribution, Physica D **406**, 132444 (2020).
[70] D. Aslangil, D. Livescu, and A. Banerjee, Effects of atwood and reynolds numbers on the evolution of buoyancy-driven homogeneous variable-density turbulence, J. Fluid Mech. **895**, A12 (2020).
[71] C. B. da Silva, The role of coherent structures in the control and interscale interactions of round, plane and coaxial jets, Ph.D. thesis, Institut National Polytechnique de Grenoble, Grenoble, France, 2001.
[72] C. B. da Silva, S. Rego, and C. F. Pereira, Analysis of the viscous/molecular subgrid-scale dissipation terms in LES based on transport equations: *A Priori* tests, J. Turbul. **9**, N25 (2008).
[73] C. B. da Silva and J. C. F. Pereira, Analysis of the gradient-diffusion hypothesis in Large-Eddy simulations based on transport equations, Phys. Fluids **19**, 035106 (2007).
[74] V. Borue and S. A. Orszag, Local energy flux and subgrid-scale statistics in three-dimensional turbulence, J. Fluid Mech. **366**, 1 (1998).
[75] S. Liu, C. Meneveau, and J. Katz, On the properties of similarity subgrid-scale models as deduced from measurements in a turbulent jet, J. Fluid Mech. **275**, 83 (1994).
[76] J. A. Saenz, D. Aslangil, and D. Livescu, Filtering, averaging and scale dependency in homogeneous variable density turbulence, Phys. Fluids **33**, 025115 (2021).
[77] B. Vreman, B. Geurts, and H. Kuerten, Realizability conditions for the turbulent stress tensor in large-eddy simulation, J. Fluid Mech. **278**, 351 (1994).
[78] U. Schumann, Subgrid scale model for finite difference simulations of turbulent flows in plane channels and annuli, J. Comput. Phys. **18**, 376 (1975).
[79] R. S. Rogallo and P. Moin, Numerical simulation of turbulent flows, Annu. Rev. Fluids Mech. **16**, 99 (1984).
[80] P. Moin, K. Squires, W. Cabot, and S. Lee, A dynamic subgrid-scale model for compressible turbulence and scalar transport, Phys. Fluids A **3**, 2746 (1991).
[81] Y. Zhou, Rayleigh-Taylor and Richtmyer-Meshkov instability induced flow, Turbulence, and Mixing. I, Phys. Rep. **720-722**, 1 (2017).
[82] Y. Zhou, Rayleigh-Taylor and Richtmyer-Meshkov instability induced flow, Turbulence, and Mixing. II, Phys. Rep. **723-725**, 1 (2017).
[83] F. S. Pereira, G. Vaz, and L. Eça, An Assessment of Scale-Resolving Simulation Models for the Flow Around a Circular Cylinder, in *Proceedings of the 8th International Symposium on Turbulence, Heat and Mass Transfer (THMT15)* (Sarajevo, Bosnia and Herzegovina, Begell House, USA, 2015), pp. 295–298.
[84] C. Kamble and S. Girimaji, Characterization of coherent structures in turbulent wake of a sphere using partially averaged Navier-Stokes (PANS) simulations, Phys. Fluids **32**, 105110 (2020).
[85] T. S. Fowler, F. D. Witherden, and S. S. Girimaji, Partially-averaged Navier-Stokes simulations of turbulent flow past a square cylinder: Comparative assessment of statistics and coherent structures at different resolutions, Phys. Fluids **32**, 125106 (2020).
[86] Y. Yang and D. I. Pullin, Evolution of vortex-surface fields in viscous Taylor-Green and Kida-Pelz flows, J. Fluid Mech. **685**, 146 (2011).
[87] N. Brachet, D. Meiron, S. Orszag, B. Nickel, R. Morf, and U. Frish, Small scale structure of the Taylor-Green vortex, J. Fluid Mech. **130**, 411 (1983).
[88] C.-W. Shu, W.-S. Don, D. Gottlieb, O. Schilling, and L. Jameson, Numerical convergence study of nearly incompressible, inviscid Taylor-Green vortex flow, J. Sci. Comput. **24**, 1 (2005).
[89] D. Drikakis, C. Fureby, F. F. Grinstein, and D. Youngs, Simulation of transition and turbulence decay in the Taylor-Green vortex, J. Turbul. **8**, N20 (2007).

[90] Y. Yang and D. I. Pullin, On lagrangian and vortex-surface fields for flows with Taylor-Green and Koda-Pelz initial conditions, J. Fluid Mech. **661**, 446 (2010).
[91] J.-B. Chapelier, M. Plata, and F. Renac, Inviscid and Viscous Simulations of the Taylor-Green Vortex Using a Model Discontinuous Galerkin Approach, in *42ndAmerican institute of Aeronautics and Astronautics (AIAA) Fluid Dynamics Conference and Exhibit*, AIAA 2012-3073 (New Orleans, LA, 2012).
[92] J. R. DeBonis, *Solutions of the Taylor-Green Vortex Problem Using High-Resolution Explicit Finite Difference Methods*, AIAA 2013-382, 51st AIAA Aerospace Sciences Meeting including the New Horizons Forum and Aerospace Exposition, 2013.
[93] I. A. Shirokov and T. G. Elizarova, Simulation of laminar-turbulent transition in compressible Taylor-Green flow basing on quasi-gas dynamic equation, J. Turbul. **15**, 707 (2014).
[94] J. R. Bull and A. Jameson, Simulation of the Taylor-Green vortex using high-order flux reconstruction schemes, AIAA J. **53**, 2750 (2015).
[95] T. Dairay, E. Lamballais, S. Laizet, and J. C. Vassilicos, Numerical dissipation vs. subgrid-scale modelling for Large Eddy simulation, J. Comput. Phys. **337**, 252 (2017).
[96] R. E. Moura, G. Mengaldo, J. Peiró, and S. J. Sherwin, On the Eddy-resolving capability of high-order discontinuous Galerkin approaches to implicit les/under-resolved DNS of Euler turbulence, J. Comput. Phys. **330**, 615 (2017).
[97] N. Peng and Y. Yang, Effects of the mach number on the evolution of vortex-surface fields in compressible Taylor-Green flows, Phys. Rev. Fluids **3**, 013401 (2018).
[98] N. Sharma and T. K. Sengupta, Vorticity dynamics of the three-dimensional Taylor-Green vortex problem, Phys. Fluids **31**, 035106 (2019).
[99] F. F. Grinstein, J. A. Saenz, J. C. Dolence, T. O. Masser, R. M. Rauenzahn, and M. M. Francois, Effects of operator splitting and low mach-number correction in turbulent mixing transition simulations, Comput. Math. Appl. **78**, 437 (2019).
[100] F. S. Pereira, F. F. Grinstein, D. M. Israel, and R. Rauenzahn, Molecular viscosity and diffusivity effects in transitional and shock-driven mixing flows, Phys. Rev. E **103**, 013106 (2021).
[101] S. Kida and M. Takaoka, Vortex reconnection, Annu. Rev. Fluid Mech. **26**, 169 (1994).
[102] A. W. Cook and P. E. Dimotakis, Transition stages of Rayleigh-Taylor instability between miscible fluids, J. Fluid Mech. **443**, 69 (2001).
[103] G. Dimonte, D. L. Youngs, A. Dimits, S. Weber, M. Marinak, S. Wunsch, C. Garasi., A. Robinson, M. J. Andrews, P. Ramaprabhu, A. C. Calder, B. Fryxell, J. Biello, L. Dursi, P. MacNeice, K. Olson, P. Ricker, R. Rosner, F. Timmes, H. Tufo *et al.*, A comparative study of the turbulent Rayleigh-Taylor instability using high-resolution three-dimensional numerical simulations: The alpha-group collaboration, Phys. Fluids **16**, 1668 (2004).
[104] J. R. Ristorcelli and T. T. Clark, Rayleigh-Taylor turbulence: Self-similar analysis and direct numerical simulations, J. Fluid Mech. **507**, 213 (2004).
[105] W. Cabot and A. Cook, Reynolds number effects on Rayleigh-Taylor instability with possible implications for type Ia supernovae, Nat. Phys. **2**, 562 (2006).
[106] A. Banerjee and M. J. Andrews, 3D simulations to investigate initial condition effects on the growth of Rayleigh-Taylor mixing, Int. J. Heat Mass Transf. **52**, 3906 (2009).
[107] D. Livescu, J. R. Ristorcelli, R. A. Gore, S. H. Dean, W. H. Cabot, and A. W. Cook, High-Reynolds number Rayleigh-Taylor turbulence, J. Turbul. **10**, N13 (2009).
[108] N. Vladimirova and M. Chertkov, Self-similarity and universality in Rayleigh-Taylor, boussinesq turbulence, Phys. Fluids **21**, 015102 (2009).
[109] D. Livescu, Numerical simulations of two-fluid turbulent mixing at large density ratios and applications to the Rayleigh-Taylor instability, Phil. Trans. R. Soc. A **371**, 20120185 (2013).
[110] D. L. Youngs, Rayleigh-Taylor mixing: Direct numerical simulation and implicit Large Eddy simulation, Phys. Scr. **92**, 074006 (2017).
[111] I. W. Kokkinakis, D. Drikakis, and D. L. Youngs, Modeling of Rayleigh-Taylor mixing using single-fluid models, Phys. Rev. E **99**, 013104 (2019).
[112] D. H. Sharp, An overview of Rayleigh-Taylor instability, Physica D **12**, 3 (1984).

[113] G. Boffeta and A. Mazzino, Incompressible Rayleigh-Taylor turbulence, Annu. Rev. Fluid Mech. **49**, 119 (2017).
[114] D. Livescu, T. Wei, and P. T. Brady, Rayleigh-Taylor instability with gravity reversal, Physica D **417**, 132832 (2021).
[115] R. E. Duff, F. H. Harlow, and C. W. Hirt, Effects of diffusion on interface instability between gases, Phys. Fluids **5**, 417 (1962).
[116] M. Gittings, R. Weaver, M. Clover, T. Betlach, N. Byrne, R. Coker, E. Dendy, R. Hueckstaedt, K. New, W. R. Oakes, D. Ranta, and R. Stefan, The RAGE radiation-hydrodynamic code, Comput. Sci. Discovery **1**, 015005 (2008).
[117] F. S. Pereira, F. F. Grinstein, and D. Israel, Effect of the numerical discretization scheme in shock-driven turbulent mixing simulations, Comput. Fluids **201**, 104487 (2020).
[118] E. F. Toro, M. Spruce, and W. Speares, Restoration of the contact surface in the HLL-Riemann solver, Shock Waves **4**, 25 (1994).
[119] P. Colella and P. R. Woodward, The piecewise parabolic method (PPM) for gas-dynamical simulations, J. Comput. Phys. **54**, 174 (1984).
[120] B. Thornber, A. Mosedale, D. Drikakis, D. Youngs, and R. J. R. Williams, An improved reconstruction method for compressible flows with low mach number features, J. Comput. Phys. **227**, 4873 (2008).
[121] F. S. Pereira, Verification of ReFRESCO with the method of manufactured solutions, M.A. thesis, Instituto Superior Técnico, Lisbon, Portugal, 2012.
[122] J. Jeong and F. Hussain, On the identification of a vortex, J. Fluid Mech. **285**, 69 (1995).
[123] B. van Leer, Towards the ultimate conservative difference scheme, J. Comput. Phys. **135**, 229 (1997).
[124] F. F. Grinstein, A. A. Gowardhan, and A. J. Wachtor, Simulations of Richtmyer-Meshkov instabilities in planar shock-tube experiments, Phys. Fluids **23**, 034106 (2011).
[125] B. M. Haines, F. F. Grinstein, and J. R. Fincke, Three-dimensional simulation strategy to determine the effects of turbulent mixing on inertial-confinement-fusion capsule performance, Phys. Rev. E **89**, 053302 (2014).
[126] D. Virk, F. Hussain, and R. M. Kerr, Compressible vortex reconnection, J. Fluid Mech. **304**, 47 (1995).